J. Fluid Mech. (2014), *vol.* 757, *pp.* 665–700.
doi:10.1017/jfm.2014.511

Model for the initiation of atomization in a high-speed laminar liquid jet

Akira Umemura†

Department of Aerospace Engineering, Nagoya University, Chikusa-ku, Nagoya 464-8603, Japan

(Received 9 December 2013; revised 27 August 2014; accepted 1 September 2014;
first published online 29 September 2014)

A laminar water jet issuing at high speed from a short circular nozzle into air exhibits various instability features at different distances from the nozzle exit. Near the exit, the effects of gaseous friction and pressure are relatively weak. Deformation of the jet surface in this region is mainly due to the instability of a thin liquid shear layer flow, which relaxes from the velocity profile produced by the nozzle wall. In this paper, a model for this type of instability based on linear stability analysis is investigated to describe the process initiating the formation of liquid ligaments disintegrating into fine droplets near the nozzle exit. The modelling comprises identifying unstable waves excitable in the liquid shear layer and exploring a self-destabilizing mechanism by which unstable waves responsible for the formation of liquid ligaments are naturally reproduced from the upstream-propagating capillary waves produced by the growth of the unstable waves themselves. An expression for the location of ligament formation onset is derived that can be compared with experiments. The model also explains changes in jet instability features away from the nozzle exit and for very short nozzles.

Key words: aerosols/atomization, capillary waves, wakes/jets

1. Introduction

Water issuing into still room air from a circular nozzle exhibits various disintegration features depending on jet speed and nozzle shape (McCarthy & Malloy 1974). At low jet speeds, the Plateau–Rayleigh (Plateau 1873; Rayleigh 1878) instability disintegrates the jet into large droplets at large distances from the nozzle. As the jet speed is increased, aerodynamic forces and the nozzle exit velocity profile affect the jet instability (Chandrasekhar 1961; Batchelor & Gill 1962; Taylor 1963; Mattingly & Chang 1974; Sterling & Sleicher 1975; Lin & Reitz 1998; Gordillo & Pérez-Saborid 2005). For a long nozzle, the nozzle flow becomes turbulent at a certain jet speed. At higher jet speeds, a fully turbulent jet experiences turbulent atomization, which transforms all the issued water into a spray of fine droplets. In contrast, a water jet issuing from a short nozzle or an equivalent convergence nozzle can maintain a laminar jet state up to a much higher jet speed. Figure 1(*a*) shows high-speed photography of such a water jet (Hoyt & Taylor 1977; Taylor & Hoyt 1983), in which the laminar velocity profile of the issued water at the nozzle exit is uniform except

† Email address for correspondence: akira@nuae.nagoya-u.ac.jp

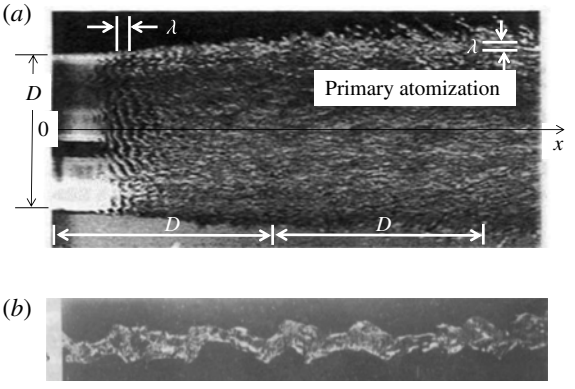

FIGURE 1. A water jet issuing into still room air at a speed of 25 m s^{-1} from a 6.35 mm diameter and 6.35 mm long straight nozzle, preceded by a cone section with a 7° half-angle. The flow exiting the nozzle is laminar. (*a*) Near the nozzle exit, appreciable axisymmetric surface deformation is observed, which develops into a three-dimensional surface deformation forming ligaments and atomized droplets. (*b*) Far downstream from the nozzle exit ($216D < x < 240D$), only relatively large-scale surface irregularities (varicose and sinuous waves) are observed.

in a thin shear flow layer adjacent to the jet surface. A characteristic instability of this jet is the emergence of fine axisymmetric surface deformation, which transitions to turbulent atomization with liquid ligaments formed almost normal to the jet surface that break into fine droplets (figure 1*a*), while the jet behaviour observed far downstream of the nozzle (figure 1*b*) is similar to that at lower jet speeds. Therefore, this jet provides a suitable prototype for studying the underlying physics initiating turbulent atomization.

The turbulent atomization mechanism has been investigated from various points of view (Ranz 1958; Mayer 1961; Taylor 1963; Reitz & Bracco 1982; ?; Levich 1992; Huh, Lee & Koo 1998; Lasheras & Hopfinger 2000; Yecko, Zaleski & Fullana 2002; Lin 2003; Marmottan & Villermaux 2004; Yecko & Zaleski 2005; Trinh 2007; Eggers & Villermaux 2008; Gorokhovski & Herrmann 2008; Shinjo & Umemura 2010, 2011) because its understanding is crucial for controlling spray formation in various applications. Most research has focused on aerodynamic effects on the interfacial instability. A well-known theory is the Kelvin–Helmholtz instability applied to an interface between liquid (density ρ, tangential velocity U, surface tension σ) and gas (ρ_g, $U_g = 0$) phases (Chandrasekhar 1961), which leads to a complex phase velocity c as a function of wavenumber k:

$$c = \frac{\rho U}{\rho + \rho_g} \pm \mathrm{i}\frac{1}{\rho + \rho_g}\sqrt{\rho\rho_g U^2 - (\rho + \rho_g)\sigma k}. \tag{1.1}$$

This expression is often used in constructing atomization simulators (typically KIVA) (Huh *et al.* 1998; Trinh 2007) for industrial applications. In this theory, the strong instability arises from a large velocity difference U between the liquid and gas phases. However, several experimental observations (Fenn & Middleman 1969; Davies & Young-Hoon 1974; Phinney 1975; Hoyt & Taylor 1977; Arai, Shimizu & Hiroyasu 1985; Karasawa *et al.* 1992; Wu, Miranda & Faeth 1995), including those shown in figure 1, indicate that aerodynamic effects on turbulent atomization are of secondary

importance. It is instead believed that a liquid shear layer formed during the nozzle passage plays an important role. Wu *et al.* (1995) showed that the size of the atomized droplets is well correlated with the liquid shear layer thickness for all tested liquids, ambient gas environments, jet exit velocities and jet exit diameters. Therefore, the interfacial instability observed in figure 1(*a*) may be independent of aerodynamic effects. However, (i) there is no theory that identifies the involved instabilities and reasonably supports this idea. Furthermore, (ii) it is not known why the turbulent atomization starts steadily at a certain distance from the nozzle exit. The present study attempts to address points (i) and (ii) by assuming a completely (disturbance-free) laminar nozzle flow.

To do this, it is necessary first to identify the origin of the liquid shear layer instability. Figure 1(*a*) indicates the temporally periodic production of small surface deformation near the nozzle exit, the spatial evolution of which may be described in a framework of linear theory. Convectively unstable shear flows (mixing layers, flat-plate wakes) are sensitive to external noise and display extrinsic dynamics (noise amplifiers) (Huerre & Monkewitz 1990). Therefore, past studies have simply assumed the presence of random disturbances from which the most unstable wave component can grow first. However, for a spatially developing instability to be periodic in time, a deterministic mechanism should exist to produce convectively unstable waves repeatedly at a fixed location. The atomization onset location will then be fixed. Considering the rapid growth of shear flow instability, it seems more reasonable to consider that the disturbances responsible for flow instability are produced downstream of the nozzle exit and the shear flow instability may be self-sustained by a deterministic mechanism.

As a linear theory describing self-sustained instabilities, the concepts of absolute instability (Briggs 1964; Huerre & Monkewitz 1990) and global mode analysis (Chomaz 2005) are familiar and applied to various flows in order to predict the baseline flow condition for which the predicted instability emerges. For example, in wakes behind a body, it is found that increased Reynolds number changes a blunt-body wake flow from a stable state to a convectively unstable state and finally an absolutely unstable state with self-excited mechanisms. In global mode analysis, the whole flow region with specific inlet and outlet boundary conditions are considered. Gallaire & Chomaz (2004) showed that wave propagations between the inlet and outlet may result in a linear instability for a simple model of incipient vortex breakdown, while most global mode analyses rely on the presence of an absolute instability region for self-sustainability.

However, these current theories do not unambiguously identify the mechanism of temporally periodic, spatially developing flow formation. In fact, the absolute instability analysis only predicts the long-time response behaviour (temporal evolution) of an impulsively forced baseline flow portion. The underlying physics of absolute instability can be easily figured out for a separated flow configuration (Yu & Monkewitz 1990; Takemoto & Mizushima 2010). When some elements of the dispersive wave produced by an impulsive forcing are elongated and turn to unstable wave elements in a region upstream of the forcing location, the disturbed flow can grow in a self-excited fashion. The baseline flow portion that exhibits such a response is called ‘absolutely unstable’. In the linear theory, any external perturbation, even part of the disturbed flow, may play a similar role as the impulsive forcing. Therefore, the disturbed flow in the absolutely unstable region must eventually be in a nonlinear regime (limit-cycle state), which can no longer be described by a linear theory (e.g. see experiments by Inoue (1985)). Although it may explain the initial

formation of convectively unstable waves, linear absolute instability does not explain the mechanism of continued periodic formation of convectively unstable waves at a fixed location unless the nonlinear dynamics is fully explored. The linear theory is only applicable to a restricted region upstream of the nonlinearly developing region. This is the place where the leading short-wave elements of the upstream-propagating dispersive wave may remain with small amplitude. Therefore, in the present study, attention is directed to a deterministic reproduction mechanism of convectively unstable waves at the nozzle exit, which is described by a linear theory, including the downstream effects caused by unstable wave growth.

In a study of low-speed water jets, in which initial Plateau–Rayleigh unstable wave elements are always in a linear regime, Umemura (2011) and Umemura *et al.* (2011) focused on the roles played by the nozzle and the upstream-propagating capillary waves (dispersive waves) produced by the surface energy release. In that work, he proposed a self-destabilizing loop that disintegrates the jet into droplets at a fixed distance according to the Plateau–Rayleigh instability. The essential idea behind this proposal is based on the fact that the end pinching and the growth of the Plateau–Rayleigh unstable wave (convective instability) is caused by the energy released by surface area reduction. Part of the released surface energy, which is transferred upstream by a capillary wave, is available to reproduce the Plateau–Rayleigh unstable wave in the newly issued liquid column.

The high-speed liquid jet in figure 1(*a*) has a common feature with this low-speed jet, in that convectively unstable waves may be reproduced in the newly issued laminar jet. The idea of a self-destabilizing mechanism developed for a low-speed liquid jet can be extended to the present problem in order to explore the self-destabilizing mechanisms involved in figure 1(*a*) by identifying the origin of the liquid shear flow instability. Figure 2 illustrates the self-destabilizing mechanism proposed in the present paper. It shows a scenario of instability initiating the formation of liquid ligaments disintegrating into fine droplets in a high-speed jet from a short nozzle. The present paper describes our theoretical developments leading to the model of figure 2 and shows the role played by the surface liquid shear layer on the excitation of atomizing ligaments.

The present paper is organized as follows. In § 2, the baseline jet flow structure of figure 1 is analysed, for which excitable instabilities are examined in the subsequent sections. In § 3, a problem involved in conventional linear instability analyses is discussed. Based on this discussion, the self-destabilizing loops proposed in figure 2 are identified in § 5 based on linear stability analysis conducted in § 4. Section 6 explains the physics underlying figures 1(*a*) and 2 and predicts the onset location of ligament formation for comparison with experimental observations. Section 7 summarizes the results of the present research.

2. Velocity profile relaxation of baseline jet flow

The jet considered in this paper is composed of water issuing into still room air from a short nozzle of diameter D and length L. Surrounding a uniform stream of large velocity U, the jet has a thin annular liquid shear layer on its surface, which is formed within the nozzle and has a thickness

$$\delta_0 = K\sqrt{\frac{\nu L}{U}} \quad (K = 3.01) \tag{2.1}$$

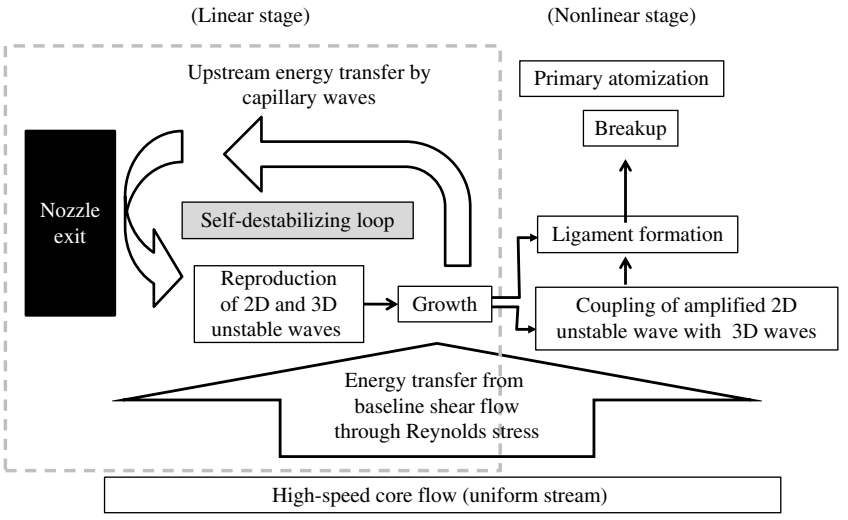

FIGURE 2. Self-destabilizing loops formed in the gaseous stress-free liquid shear flow layer. These loops initiate turbulent atomization. The present paper mainly treats the linear stage enclosed by the grey dashed line. The unstable waves excited in the shear layer gain energy from the high-speed core flow through the Reynolds stress and then grow. The growth of an unstable wave produces capillary waves, which propagate and transport energy upstream and downstream. Short-wavelength capillary waves reaching the nozzle exit reflect and may turn to the unstable waves by the Doppler effect at the nozzle exit, thus reproducing the unstable waves, which generate the short-wavelength capillary waves. The three-dimensional unstable waves are amplified to form ligaments that disintegrate into droplets. This process is nonlinear and generates various waves, which prevents deterministic tracking of the flow development. Overall, the energy cascades from the high-speed core flow towards atomized droplets.

at the nozzle exit $x=0$, where the value of K is determined using the Blasius solution (Schlichting 1968) such that the boundary layer thickness is equal to the ratio of the uniform stream velocity and the velocity gradient at the nozzle wall.

The gas density ρ_g is much smaller than the liquid density ρ. The steady laminar jet flow (baseline jet flow for stability analysis) realized in the absence of any instability is characterized as follows. Owing to the liquid kinematic viscosity $\nu=\mu/\rho$, the liquid shear layer relaxes to that compatible with the gaseous frictional stress. At the nozzle exit $x=0$, where the surface velocity $U_s(x)$ is zero, gaseous stress does not act on the jet. As the surface velocity increases downstream, the gaseous stress gradually increases. In the vicinity of the nozzle exit, the relatively low surface velocity allows us to consider that the velocity profile of the liquid shear layer relaxes as if the jet surface were free from gaseous stress. Therefore, the jet surface velocity U_s increases from zero towards the uniform velocity U.

Since the shear layer thickness δ_0 is much smaller than the nozzle diameter D, the liquid shear layer flow may be regarded as planar. In fact, in the experimental condition of figure 1, application of (2.1) to the straight nozzle section leads to $\delta_0/(D/2)=0.016$. This result will not change significantly even if the boundary layer formed in the convergent nozzle section is taken into account. Thus, to characterize the shear layer flow, it is assumed that the water occupies a semi-infinite region $x>0$ and $y>0$. At the nozzle exit location $x=0$, the water has an axial velocity

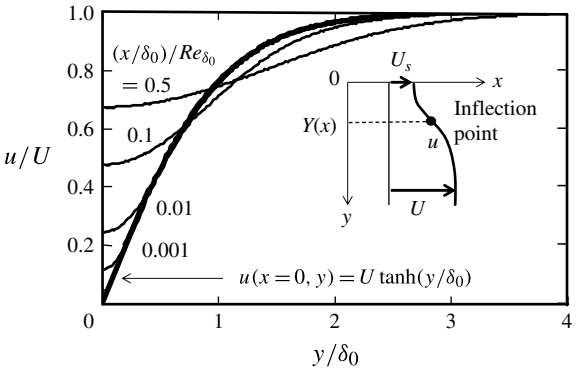

FIGURE 3. Velocity profile relaxation of the jet surface flow layer. The axial velocity component u at a distance x from the nozzle exit is expressed as a function of distance y from the jet surface as shown by the inset. The Reynolds number $Re_{\delta_0} = U\delta_0/\nu$ is based on the initial layer thickness δ_0 and uniform core flow velocity U.

profile $u = U\tanh(y/\delta)$, while the stress-free condition $\partial u/\partial y = 0$ is satisfied along the surface $y = 0$. The steady parallel flow, governed by a unidirectional flow equation $u\,\partial u/\partial x = \nu\,\partial^2 u/\partial y^2$, was solved numerically under the above-mentioned boundary conditions to describe the velocity profile relaxation along the jet. This equation neglects the term $v\,\partial u/\partial y$ in the boundary layer equation, but this approximation does not affect the flow structure in an essential way. The relevant dimensionless parameter is the Reynolds number defined by

$$Re_{\delta_0} = \frac{U\delta_0}{\nu}. \tag{2.2}$$

Figure 3 shows the change in axial velocity profile along the jet. Dragged by the high-speed core flow, the surface gains a velocity $U_s(x) = u(x, y = 0)$. The velocity profile has an inflection point at a distance $Y(x)$ from the surface at each location x along the jet. The variations of Y and U_s with x from numerical solutions are shown in figure 4. They are found to be correlated by

$$\frac{U_s}{U} = \frac{1}{2}\left(\frac{Y}{\delta_0}\right)^{4/3} = \frac{1}{2}\left[\frac{10}{Re_{\delta_0}}\left(\frac{x}{\delta_0}\right)\right]^{1/3}. \tag{2.3}$$

Using (2.1) and (2.2), the abscissa of figure 4 can be rewritten as

$$\frac{1}{Re_{\delta_0}}\frac{x}{\delta_0} = \frac{1}{K^2}\frac{D}{L}\frac{x}{D}. \tag{2.4}$$

Note that the value of U_s/U at each x does not depend on the jet speed U.

3. Energetic consideration of disturbed flow

Instabilities excitable for the baseline jet flow can be examined within the framework of linear stability analysis. However, there is an important issue that is not addressed enough in conventional methods. Before presenting our linear stability analysis, we explain this issue in this section in the context of the present two-phase

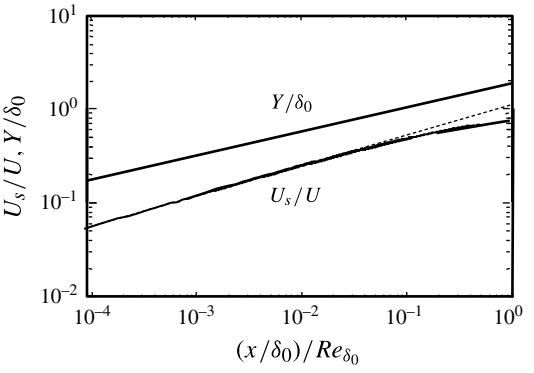

FIGURE 4. Numerical characterization of jet surface flow layer (solid lines). Here U_s is the surface velocity; and Y is the distance from the surface to the inflection point of the axial velocity profile. The dotted lines correspond to (2.3).

flow problem, although the following arguments are applicable to other problems as well (including nozzle flows).

Figure 5 shows a control volume (labelled CDFE), set at a distance X from the nozzle exit. We assume that both liquid and gas flows are governed by the incompressible Navier–Stokes equations for velocity $v_i = u\delta_{ix} + v_i'$, pressure $p = 0 + p'$ and surface deformation $\eta = 0 + \eta'$. Integrating the inner product of the Navier–Stokes equations and the velocity v_i over the control volume leads to the following expression (written in two dimensions only for clarity) for the conservation of the sum of kinetic energy and surface energy:

$$\begin{aligned}
&\frac{\mathrm{d}}{\mathrm{d}t}\Bigg[\underbrace{\iint_{\mathrm{CDFE}} \frac{\rho v_i^2}{2}\,\mathrm{d}x\,\mathrm{d}y}_{\text{kinetic energy}} + \underbrace{\sigma\int_X^{X+\Delta x}\sqrt{1+\left(\frac{\partial\eta}{\partial x}\right)^2}\,\mathrm{d}x}_{\text{surface energy}}\Bigg] \\
&\quad = \underbrace{\iint_{\mathrm{CDFE}} \rho v_i v_j \frac{\partial v_i}{\partial x_j}\,\mathrm{d}x\,\mathrm{d}y}_{Q} - \underbrace{\iint_{\mathrm{CDFE}} \mu\left(\frac{\partial v_i}{\partial x_j}\right)^2\,\mathrm{d}x\,\mathrm{d}y}_{\text{dissipation energy}} \\
&\qquad + \underbrace{\int_{\mathrm{CE}}\left[\left(\frac{\rho v_i^2}{2}+p\right)v_x - \frac{1}{2}\mu\frac{\partial v_i^2}{\partial x}\right]\mathrm{d}y}_{J_-} + \underbrace{\left\{-\int_{\mathrm{DF}}\left[\left(\frac{\rho v_i^2}{2}+p\right)v_x - \frac{1}{2}\mu\frac{\partial v_i^2}{\partial x}\right]\mathrm{d}y\right\}}_{J_+} \\
&\qquad + \underbrace{\left\{-\sigma\left.\frac{\frac{\partial\eta}{\partial x}\frac{\partial\eta}{\partial t}}{\sqrt{1+\left(\frac{\partial\eta}{\partial x}\right)^2}}\right|_{x=X}\right\}}_{W_-} + \underbrace{\sigma\left.\frac{\frac{\partial\eta}{\partial x}\frac{\partial\eta}{\partial t}}{\sqrt{1+\left(\frac{\partial\eta}{\partial x}\right)^2}}\right|_{x=X+\Delta x}}_{W_+}.
\end{aligned} \tag{3.1}$$

If we take an ensemble average of (3.1) and subtract the baseline flow contributions, we obtain the conservation equation for the sum of the kinetic energy and surface energy of the disturbed flow. In this averaged equation, the term Q expresses the

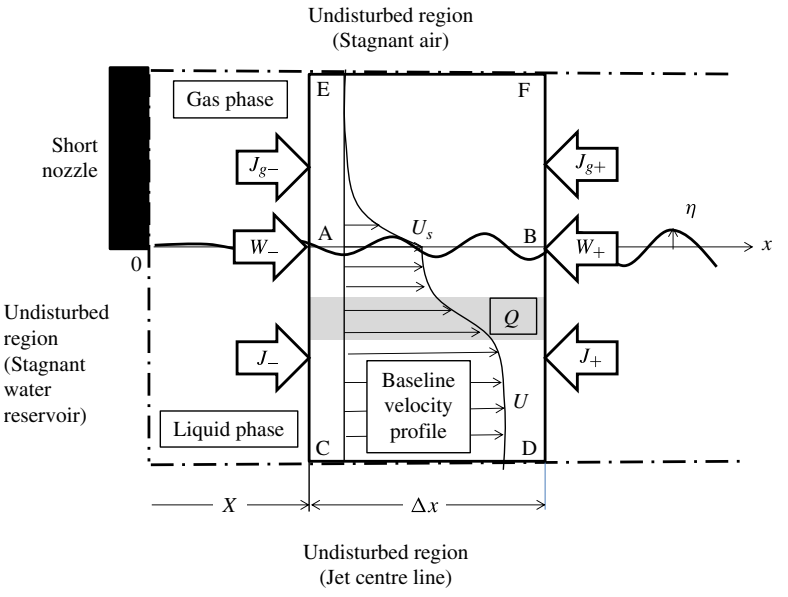

FIGURE 5. Energy balance for fluid in a control volume. The x axis is taken to be consistent with the liquid surface of the baseline jet flow. In general, the fluid receives energy transferred from outside the control volume. In the grey region, the disturbed flow gains energy Q from the baseline jet flow through the Reynolds stress. Since an objective of the present study is to show that turbulent atomization can be brought about without the influence of gaseous flow, $J_{g-} = J_{g+} = 0$ is assumed in the text.

energy transferred from the baseline flow to the disturbed flow through the Reynolds stress. There are no energy influxes from undisturbed regions. Equation (3.1) clearly indicates that disturbed flow develops by receiving energy not only from Q but also from W and J, which express the energy transferred from upstream and downstream of the control volume. As a result, even if the control volume and its upstream region are initially in an undisturbed flow state ($Q = W_- = J_- = 0$), a disturbed flow can be produced in the control volume by the presence of W_+ and J_+ as a result of (i) penetration of a disperse capillary wave due to the surface deformation of the downstream disturbed flow and (ii) formation of an induced flow field due to the vorticity distribution of the downstream disturbed flow.

When the x directional variation of the baseline flow can be neglected in the control volume, linear stability of the local baseline flow can be examined by conventional stability analysis, which assumes that the disturbed flow has an x dependence of $\exp(\mathrm{i}kx)$. However, the resulting unstable wave solution (in either temporal or spatial evolution analysis) does not generally satisfy the boundary conditions associated with W and J. This is because the unstable wave solution accounts for the effect of Q but does not correctly account for the resulting effects of W and J, even in the linear regime. This difficulty becomes serious especially where the unstable wave has the smallest amplitude, i.e. where the unstable wave is produced in a newly issued liquid ($W_- = J_- = 0$). To resolve this difficulty, we need an additional solution that accounts for the presence of W_+ and J_+. That is a neutral wave solution that transports energy effectively from the downstream side and produces an unstable wave in the newly issued liquid.

Umemura (2011) introduced this self-destabilizing mechanism to modify the conventional linear instability analysis for low-speed jets, in which the reduction in surface area is the only source of energy for the unstable wave. He showed that the steady reproduction of the Plateau–Rayleigh unstable wave in the newly issued liquid can be described by introducing a synchronized steady capillary wave that transports a portion of the surface energy released by the growth of the Plateau–Rayleigh unstable wave or by jet tip contraction, in the upstream direction. A similar mechanism might operate for the high-speed laminar jet considered in the present study. We note the presence of W_+ in a disturbed flow region. A capillary wave intrinsic to two-phase flow is indispensable for the onset of turbulent atomization. In addition, similar to the Love waves (see Love 1911) found in elasticity problems, the capillary wave may be an effective energy transport agent because the involved liquid region is confined to a thin surface liquid layer along the jet surface. Therefore, it is conjectured that a rapid growth of an unstable wave near the nozzle exit produces dispersive capillary waves propagating in the upstream direction and disturbing the newly issued liquid.

To examine this possibility, we first analyse the types of unstable and neutral waves that are excitable at each station along the baseline jet flow in § 4. This analysis can be carried out following a conventional linear stability analysis. To determine which waves are really excited within the control volume targeted by the linear stability analysis, we have to examine the downstream boundary state of the control volume (presence of W_+ and J_+). If there is significant energy transfer across the downstream boundary, the control volume state must count this energy flux. Such a consideration is indispensable in the present stability analysis, because unstable wave growth results in a nonlinear flow downstream and there must emerge dispersive capillary waves propagating in the upstream direction. In § 5, the perturbation wave characteristics derived from the linear stability analysis in § 4 are combined with this control volume argument to propose a mechanism by which the convectively unstable waves derived from the linear stability analysis are naturally reproduced periodically at the nozzle exit.

4. Linear stability analysis of baseline jet flow

In a linear system, a temporally periodic phenomenon must be described in terms of synchronized waves. The linear spatial stability of the baseline flow at each axial location $x = X$ can be examined by imposing on the local baseline flow field $\{[u(X, y), 0, 0], p = 0\}$, a perturbation flow

$$(u', v', w', p') = \{\bar{u}'(y), \bar{v}'(y), \bar{w}'(y), \bar{p}'(y)\} \exp[\mathrm{i}k\xi - \mathrm{i}\omega t + \mathrm{i}mz] \tag{4.1}$$

and surface deformation

$$\eta = \varepsilon \exp[\mathrm{i}k\xi - \mathrm{i}\omega t + \mathrm{i}mz], \tag{4.2}$$

where k, m and ω denote the complex axial wavenumber $(k_r + \mathrm{i}k_i)$, real azimuthal wavenumber and real frequency, respectively. Here ξ is the local axial coordinate defined about each axial location $x = X$ and z is the coordinate perpendicular to the xy plane. The local baseline flow is assumed to be uniform in the axial direction. The disturbed flow must satisfy the following energy conservation equation:

$$\left[\frac{\partial}{\partial t} + u(y)\frac{\partial}{\partial \xi}\right] \frac{\rho(u'^2 + v'^2)}{2} = -\frac{\partial u'p'}{\partial \xi} - \frac{\partial vp'}{\partial y} - \rho u'v'\frac{\mathrm{d}u}{\mathrm{d}y}. \tag{4.3}$$

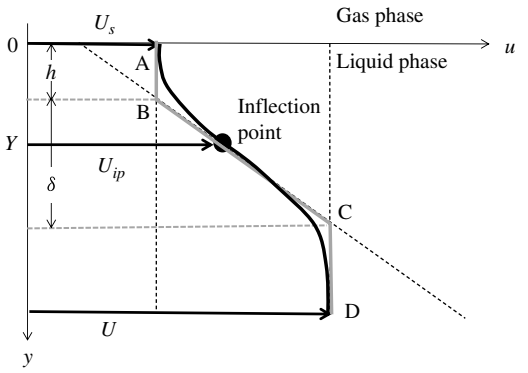

FIGURE 6. Modelling of the local axial velocity profile (black line) of the liquid shear layer. The broken-line profile (grey line) defines a three-layer structure. The values of the characteristic quantities, U_s, Y, h and δ, change with the distance x from the nozzle exit.

This indicates that the unstable wave can grow only when energy is supplied from the shear flow ($\partial u/\partial y > 0$) through the Reynolds stress (the third term on the right-hand side). Therefore, if $\partial u/\partial y = 0$ or the perturbation velocity vanishes where the shear rate exists, the perturbation wave must be a neutral wave.

4.1. *Modelled velocity profile*

Based on figure 3, the baseline jet flow at each U_s location was approximated by the following analytical expression:

$$\hat{u} = \frac{u - U_s}{U - U_s} = \begin{cases} \psi y^2, & 0 \leqslant y \leqslant Y, \\ \tanh\left(\dfrac{y-\theta}{\delta_*}\right), & y \geqslant Y. \end{cases} \tag{4.4}$$

The parameters ψ and θ are determined so as to make the velocity profile and its slope continuous at the inflection point $y = Y$:

$$\psi = \frac{-\delta_* + \sqrt{\delta_*^2 + Y^2}}{Y^3}, \quad \frac{\theta}{\delta_*} = \frac{Y}{\delta_*} - \frac{1}{2}\ln\left|\frac{1 - \dfrac{Y}{\delta_*} + \sqrt{1 + \left(\dfrac{Y}{\delta_*}\right)^2}}{1 + \dfrac{Y}{\delta_*} - \sqrt{1 + \left(\dfrac{Y}{\delta_*}\right)^2}}\right|. \tag{4.5a,b}$$

The grey solid line in figure 6 expresses the broken-line profile (three-layer model) (Rayleigh 1880). The parameters δ_* and Y are related to the parameters h and δ as follows:

$$\frac{Y}{\delta_0} = 2\frac{h}{\delta_0} = \begin{cases} 2\dfrac{U_s}{U}, & 0 \leqslant \dfrac{U_s}{U} \leqslant \dfrac{1}{2}, \\ \dfrac{1}{2}\dfrac{1}{1 - \dfrac{U_s}{U}}, & \dfrac{1}{2} \leqslant \dfrac{U_s}{U} \leqslant 1, \end{cases} \tag{4.6}$$

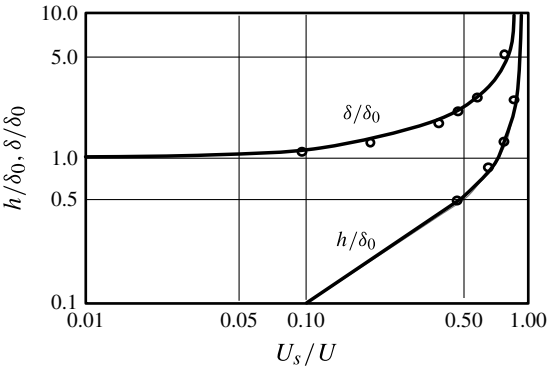

FIGURE 7. Axial change in the liquid shear layer structure modelled in figure 6. Instead of the distance x from the nozzle exit, the dimensionless surface velocity U_s/U is used to express the degree of velocity profile relaxation. The open circles denote the correlation equations $\delta/\delta_0 = 1/[1-(U_s/U)]$ and $h/\delta_0 = U_s/U$ $(0 \leqslant U_s/U \leqslant 0.5)$ or $0.25/[1-(U_s/U)]$ $(0.5 \leqslant U_s/U \leqslant 1)$.

$$\frac{\delta_*}{\delta_0} = \frac{\delta}{\delta_0} - \frac{\left(\dfrac{h}{\delta_0}\right)^2}{\dfrac{\delta}{\delta_0}} = \begin{cases} \dfrac{1}{1-\dfrac{U_s}{U}} - \left(\dfrac{U_s}{U}\right)^2\left(1-\dfrac{U_s}{U}\right), & 0 \leqslant \dfrac{U_s}{U} \leqslant \dfrac{1}{2}, \\ \dfrac{15}{16}\dfrac{1}{1-\dfrac{U_s}{U}}, & \dfrac{1}{2} \leqslant \dfrac{U_s}{U} \leqslant 1. \end{cases} \tag{4.7}$$

Figure 7 shows the correlations of h and δ with the numerical calculation results.

It is known (Rees & Juniper 2009) that the exact shape of the baseline velocity profile does not qualitatively change its stability characteristics and only weakly changes the cutoff wavenumber above which perturbations are neutralized. This fact was confirmed in our preliminary stability analyses. This would be the case, whether viscous or inviscid, as confirmed in the single shear problem (Esch 1957).

4.2. *Spatial evolution analysis*

The jet surface deformation introduces the Weber number

$$We_{\delta_0} = \frac{\rho U^2 \delta_0}{\sigma} \tag{4.8}$$

into the stability analysis. For a given set of dimensionless parameters We_{δ_0}, U_s/U, $m\delta_0$ and $\omega\delta_0/U$, we solved the following ordinary differential equation system (transformed from the Rayleigh equation, i.e. the homogeneous type of (B 9) for $\bar{p}' = P_k$) numerically to determine the eigenvalue $k\delta_0$:

$$\Pi = \frac{1}{\bar{p}'}\frac{\mathrm{d}\bar{p}'}{\mathrm{d}y}, \tag{4.9}$$

$$\frac{\mathrm{d}\Pi}{\mathrm{d}u} - 2\frac{k}{ku-\omega}\Pi + \frac{\Pi^2 - (k^2+m^2)}{\mathrm{d}u/\mathrm{d}y} = 0, \tag{4.10}$$

$$\Pi(y=\infty \text{ or } u=U) = -\sqrt{k^2+m^2}, \tag{4.11}$$

$$\Pi(y=0 \text{ or } u=U_s) = \frac{\rho(kU_s-\omega)^2}{\sigma(k^2+m^2)} = \frac{1}{\delta_0}\frac{\left(k\delta_0\dfrac{U_s}{U}-\dfrac{\omega\delta_0}{U}\right)^2}{(k\delta_0)^2+(m\delta_0)^2}\frac{1}{We_{\delta_0}}, \tag{4.12}$$

where, from (4.4),

$$\frac{\mathrm{d}\hat{u}}{\mathrm{d}y} = \begin{cases} 2\sqrt{\psi\hat{u}}, & 0\leqslant y\leqslant Y, \\ \dfrac{1}{\delta_*}[1-\hat{u}^2], & y\geqslant Y. \end{cases} \tag{4.13}$$

Equation (4.10) can be integrated from $u=U$ towards $u=U_s$ subject to the boundary condition (4.11) and $\mathrm{d}\Pi/\mathrm{d}u(u=U) = -2\sqrt{k^2+m^2}/(1+\delta_*\sqrt{k^2+m^2})(U-\omega/k)$. The eigenvalue k is determined so as to satisfy the boundary condition (4.11) at $u=U_s$. In the limiting case $We_{\delta_0}\to\infty$, when $\bar{p}'(y=0)=0$ and therefore Π diverges at $y=0$, the solution is obtained by replacing Π by $f=1/\Pi$ in the system of equations.

The following are found from this system of equations. If the liquid region is extended symmetrically about $y=0$ to the other semi-infinite space $y<0$ with the same velocity profile as (4.4), this baseline flow expresses a wake flow behind a flat plate placed parallel to a uniform liquid stream of velocity U. The inviscid stability of this flow is governed by the same differential equation as (4.10) subject to the boundary conditions $\Pi(y=\pm\infty) = \mp\sqrt{k^2+m^2}$. It is well known that wake flow has two instability modes: the varicose mode satisfying $\Pi(y=0)=0$, and the sinuous mode satisfying $|\Pi(y=0)|=\infty$. The latter mode has a larger growth rate than the former (Papageorgiou & Smith 1989; Woodley & Peake 1997; Taylor & Peake 1999). The surface boundary condition (4.12) implies that $\Pi(y=0)\to 0$ as $We_{\delta_0}\to 0$ while $\Pi(y=0)$ diverges as $We_{\delta_0}\to\infty$ in which we are interested. Therefore, our baseline jet flow has an unstable wave solution corresponding to the sinuous mode of a flat-plate wake. In our problem, the sinuous mode corresponds to a deformable jet surface while the varicose mode corresponds to no jet surface deformation. Thus, jet surface deformation is indispensable for the excitation of a strong liquid shear flow instability at large We_{δ_0}, which leads to the onset of atomization downstream. Therefore, only solutions at large We_{δ_0} are presented in the following. Furthermore, the spatial unstable solutions being presented are those which can transform to the temporal unsteady solutions by an increase in the imaginary part ω_i of the complex frequency $\omega=\omega_r+\mathrm{i}\omega_I$ (causality).

In the present study, the liquid issued from the nozzle is assumed to be in a laminar flow state to ensure the exclusion of unknown nozzle flow disturbances responsible for the liquid shear flow instability. Therefore, the experimentally allowable value of Re_{δ_0} or We_{δ_0} has an upper limit for a long nozzle. In the case of figure 1, $Re_{\delta_0}=1196$ and $\rho\nu U/\sigma = We_{\delta_0}/Re_{\delta_0} = 0.347$. The estimated Reynolds number Re_{δ_0} exceeds the critical Reynolds number of 735 (corresponding to 420 in Schlichting (1968)) for the stability of wall boundary layer flow, but it is still smaller than the turbulent transition Reynolds number of 1663 (quoted as 950 in Schlichting (1968)). The condition $Re_{\delta_0} = \sqrt{We_{\delta_0}}\times\sqrt{(\sigma\delta_0)/\rho}/\nu < 735$ leads to $We_{\delta_0}<148$ for figure 1(*a*). Thus, we will select $We_{\delta_0}=100$ as a typical value in the present study in order to allow for a long nozzle. However, the model developed in the present study will be able to apply larger Re_{δ_0} values to describe a self-destabilizing mechanism operating in the near-nozzle region of a short nozzle.

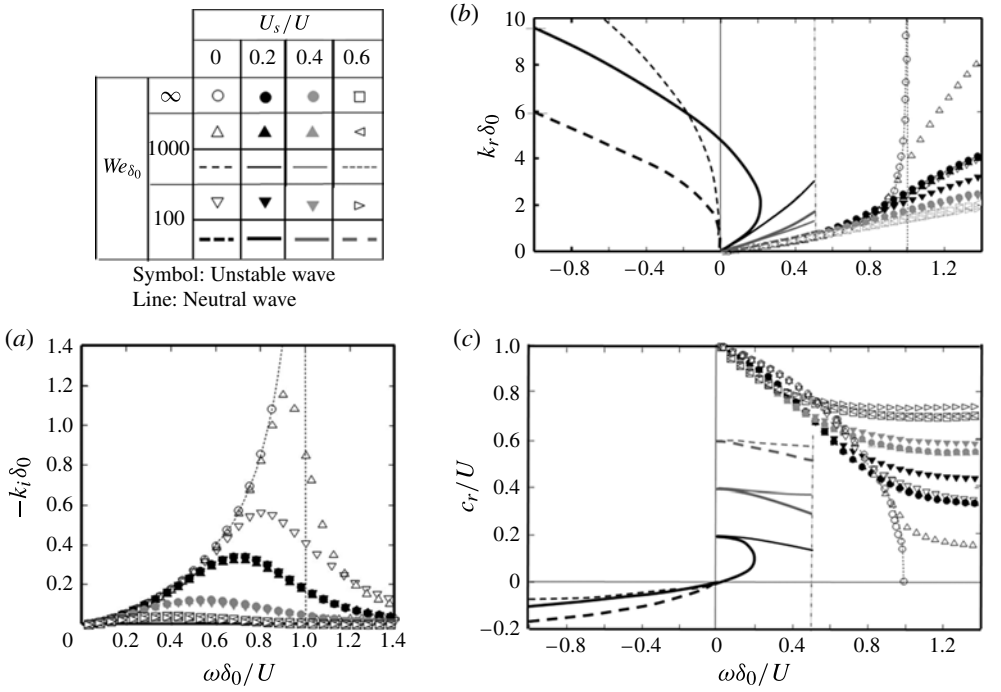

FIGURE 8. The 2D spatial instability characteristics along the jet: (*a*) spatial growth rate; (*b*) wavenumber; (*c*) phase velocity. The phase velocity c_r is calculated by dividing the frequency ω by the real wavenumber k_r.

4.3. *Two-dimensional stability*

First, we consider two-dimensional (2D) perturbations ($m = 0$). The parameter U_s/U specifies a location x along the jet by (2.3). For given values of We_{δ_0} and U_s/U, the complex eigenvalue $k = k_r + \mathrm{i}k_i$ is calculated as a function of frequency ω. Figure 8 shows the local stability characteristics at four locations $U_s/U = 0$, 0.2, 0.4 and 0.6 for $We_{\delta_0} = \infty$, 1000 and 100. All quantities are non-dimensionalized. The dependence of spatial growth rate ($-k_i$), real wavenumber k_r and phase velocity $c_r = \omega/k_r$ on frequency ω are depicted in figure 8(*a*), (*b*) and (*c*), respectively. These behaviours are similar to the sinuous mode of a wake flow with a Gaussian velocity profile, except in a vicinity of $U_s/U = 0$, where there appears a singular behaviour intrinsic to the present problem (which will be discussed later). The presence of surface tension suppresses instability and results in smaller growth rate. However, this decrement is not significant at large $We_{\delta_0} > 50$, except in the vicinity of $U_s/U = 0$ in the limit $We_{\delta_0} \to \infty$. The maximum growth rate decreases as the surface velocity increases, owing to the shear rate decrease. Note that all waves shown in figure 8 are associated with sinusoidal jet surface deformation. By phase mixing, the influence of a sinusoidal surface deformation of wavenumber k_r is confined within a distance of $O(1/k_r)$ from the surface. In the three-layer model (see figure 6), the baseline flow state is clearly distinguished by the boundary distances h and $h + \delta$ from the surface. The Reynolds stress contribution is active only in the layer $h < y < h + \delta$. Therefore, for a wave satisfying $kh > 1$, the wave cannot obtain energy from the shear flow (see (4.3)). As a result, the unstable wave turns to a neutral wave at a cutoff wavenumber depending

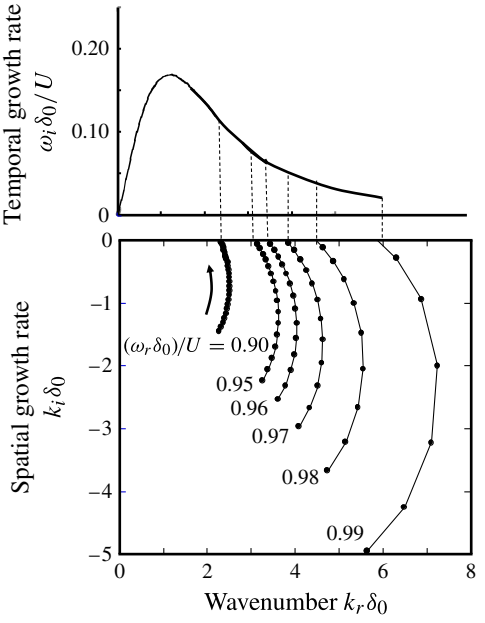

FIGURE 9. Relationship between spatial and temporal evolution solutions for $U_s = 0$ and $We_{\delta_0} = \infty$. The solid circles denote the complex wavenumber $k = k_r + \mathrm{i}k_i$ obtained when the imaginary part ω_i of complex frequency ω is increased by an increment of $0.05U/\delta_0$ for each prescribed real part ω_r.

on U_s/U (and We_{δ_0}). Unlike the unstable wave with a wavenumber dependence on frequency almost independent of We_{δ_0} and U_s/U, the neutralized wave (capillary wave) is significantly affected by We_{δ_0} and U_s/U.

There is another class of capillary wave solution, which is shown by a line with no symbols in figure 8(*b*,*c*) for the frequency range $\omega\delta_0/U < 0.5$. This capillary wave has an upstream propagation speed. As the wavenumber increases, the phase velocity decreases from U_s and eventually becomes negative. In figure 8, the range of ω is extended to the negative side to express the upstream-propagating capillary wave portion continuously, although both real frequency ω and wavenumber k_r are assumed to take a non-negative value in the text. The upstream-propagating capillary wave satisfies the dispersion relation $\omega = k'(\sqrt{\sigma k'/\rho} - U_s)$ to a good approximation except immediately near the nozzle exit. According to (3.1), the upstream energy transfer rate of this wave with small amplitude ε is calculated as

$$E = J_+ + W_+ = \frac{\omega}{2\pi}\int_0^{2\pi/\omega}\left[-\int_{-\infty}^{0}\left\{p'u' + \frac{1}{2}\rho(u'^2 + v'^2)U_s\right\}\mathrm{d}y + \sigma\frac{\partial\eta_c}{\partial x}\frac{\partial\eta_c}{\partial t}\right]\mathrm{d}t = \frac{3\sigma}{4}\varepsilon^2 k\omega. \tag{4.14}$$

At $U_s = 0$ ($h = 0$) in the limit $We_{\delta_0} \to \infty$, the unstable wave covers all wavenumbers and exhibits singular behaviour characterized by $-k_i\delta_0 = 0.52/\sqrt{1-(\omega\delta_0/U)}$, $k_r\delta_0 = 0.75/\sqrt{1-(\omega\delta_0/U)}$ and $c_r/U = 1.33\sqrt{1-(\omega\delta_0/U)}$. This singularity is intrinsic to the present baseline shear flow. Figure 9 shows the traces of the complex wavenumber k obtained when we consider a complex frequency $\omega = \omega_r + \mathrm{i}\omega_i$ and

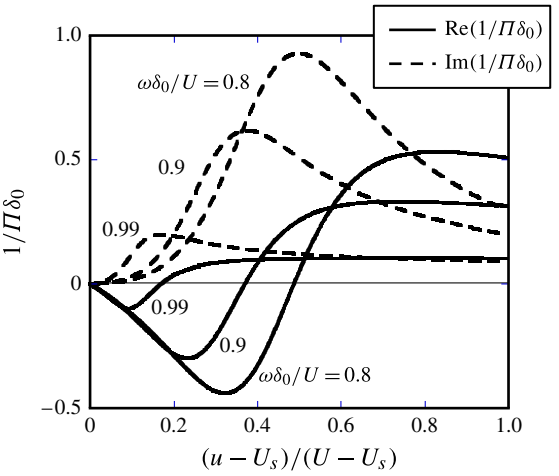

FIGURE 10. Solution of (4.10)–(4.12) for $U_s = 0$ and $We_{\delta_0} = \infty$. The critical layer location where $k_r u - \omega$ becomes zero is consistent with the zero point of the real part of $1/\Pi$. As $\omega\delta_0/U$ approaches unity, the critical layer approaches the jet surface.

increase the imaginary part ω_i from zero. Since the spatial solution transitions to the temporal solution, it is confirmed that the calculated solutions express the growing wave. In figure 9, the temporal growth rate distribution over wavenumber is also plotted, which has a long tail extending to infinite k_r. In either spatial or temporal solutions, the phase velocity approaches zero as k_r tends to infinity. As a result, even for a very small temporal growth rate, the vanishingly small travelling distance of a convectively unstable wave element during a long time results in a large spatial growth rate diverging at the condition $\omega\delta_0/U = 1$. As U_s increases from zero, this singularity disappears because h increases from zero. Figure 10 shows the change in the $1/\Pi$ profile with $\omega\delta_0/U$. It is found that the critical layer location approaches the surface as $\omega\delta_0/U$ approaches unity (and thereby k_r diverges). For $U_s > 0$, the critical layer for large k_r should be at $u < U_s$, so that no unstable wave exists at large wavenumbers.

4.4. *Three-dimensional stability*

Figure 11 shows three-dimensional (3D) unstable waves ($m\delta_0 = 0$, 0.5, 1 and 2) at $U_s/U_\infty = 0$, 0.2, 0.4 and 0.6 for $We_{\delta_0} = 100$. The overall trend at $U_s/U_\infty > 0$ is similar to the 2D case. An additional azimuthal surface tension action further suppresses instability and reduces the growth rate and cutoff wavenumber as $m\delta_o$ increases. On the other hand, it is interesting to note that the introduction of azimuthal surface deformation causes the upstream-propagating capillary wave velocity to diverge at vanishingly small ω or k_r. This effect is a consequence of the fact that purely azimuthal capillary waves ($k_r = 0$) can propagate in the azimuthal direction independently of the baseline jet flow. As a result, the 3D unstable waves have a lower limit to wavenumber that increases with m. Because of this narrowing of the unstable wave range, the 3D unstable waves with large m have a smaller growth rate and cannot play an important role in jet instability. In figure 11, the 3D unstable wave with $m = k_r$ is also depicted for reference, which will be used to consider ligament formation from the jet surface in § 6. The maximum growth rate of the 3D unstable wave is smaller than that of the 2D unstable wave.

https://doi.org/10.1017/jfm.2014.511 Published online by Cambridge University Press

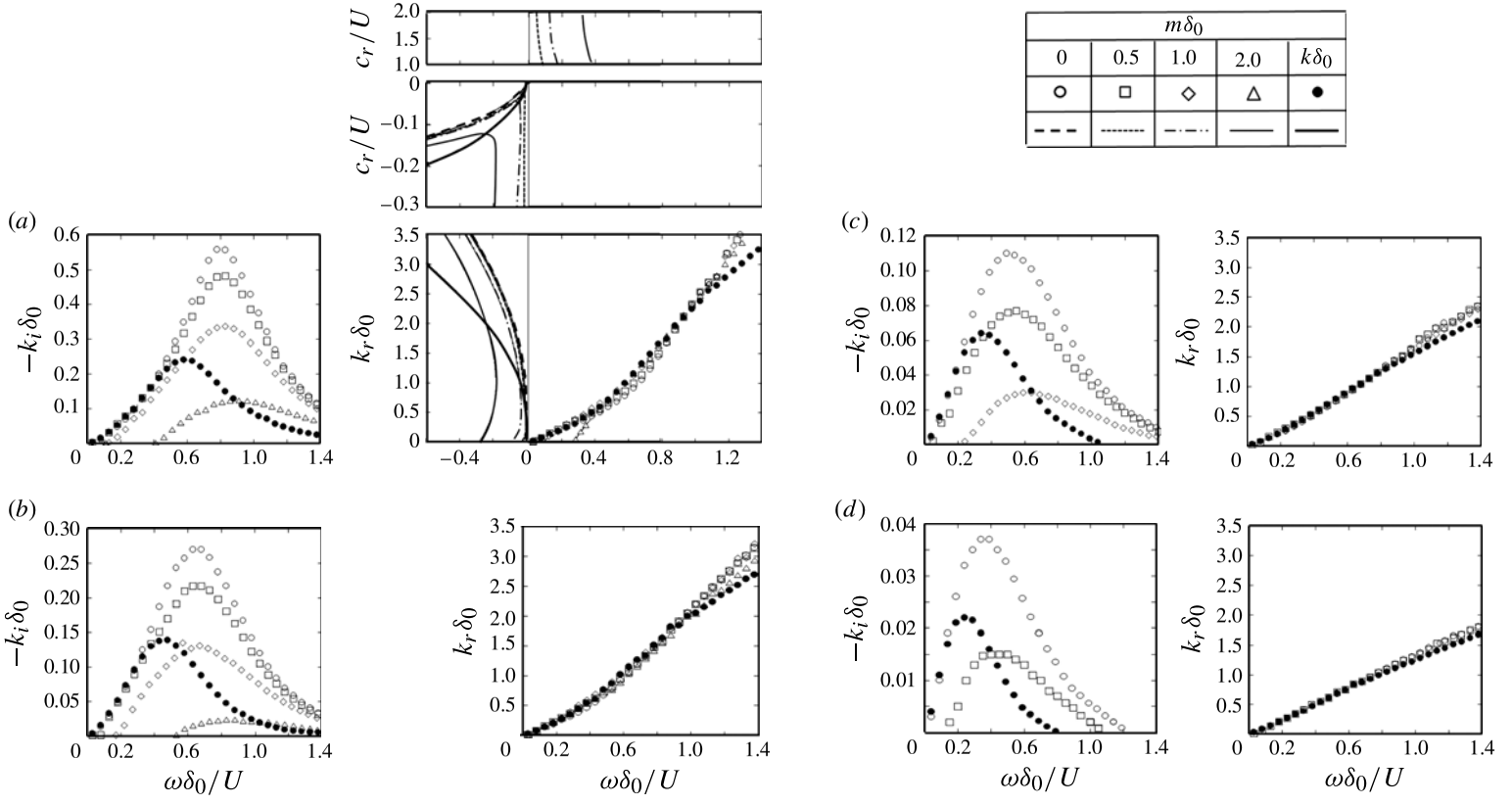

FIGURE 11. The 3D spatial instability characteristics along the jet at $We_{\delta_0} = 100$: (*a*) $U_s/U = 0$; (*b*) $U_s/U = 0.2$; (*c*) $U_s/U = 0.4$; (*d*) $U_s/U = 0.6$. The dimensionless spatial growth rate $(-k_i\delta_0)$ and axial wavenumber $k_r\delta_0$ are expressed as functions of the dimensionless frequency $\omega\delta_0/U$. The dimensionless azimuthal wavenumber $m\delta$ is taken as a parameter. This figure should be compared to the graphs at $We_{\delta_0} = 100$ in figure 8(*a*,*b*).

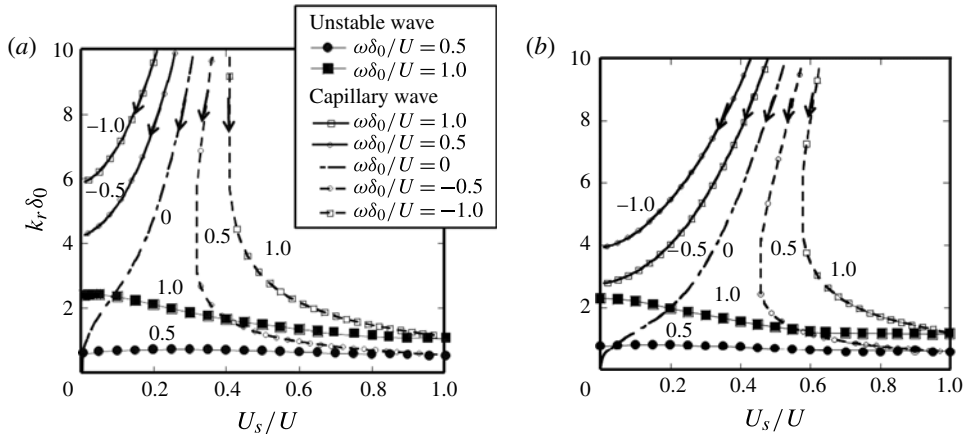

FIGURE 12. Change in wavenumber of (*a*) 2D and (*b*) 3D ($m = k$) synchronized neutral and unstable waves along the jet at $We_{\delta_0} = 100$. Energy is transferred along each capillary wave curve in the direction indicated by the arrows. Each unstable wave transforms to a neutral wave at a larger distance from the nozzle for smaller wavenumber.

An important indication in figures 8 and 11 is that the liquid shear layer may become unstable without any assistance of aerodynamic forces. Unlike the low-speed jet, in which the Plateau–Rayleigh instability is sustained by a decrease in surface area, the present unstable waves that increase the jet surface area are sustained by the Reynolds stress, which transfers energy from the baseline jet flow to the disturbed flow. We also note that the unstable wave solutions are only applicable when the jet surface can deform. If the liquid surface is not allowed to deform, such as for pipe flow, no unstable wave exists at the large We_δ value under consideration. Therefore, the unstable waves at the large Weber number, derived in this analysis, describe those unstable waves characteristic to high-speed liquid jets with a thin liquid shear layer on the jet surface.

5. Self-destabilizing mechanism

The convectively unstable waves predicted by the linear stability analysis can emerge only when their initial wave elements are produced at a fixed location somehow. To explain why the liquid jet issued in a laminar flow state can exhibit a 'steadily' atomizing feature (figure 1*a*), it is necessary to explore the mechanism by which the convectively unstable waves are steadily reproduced at a fixed location near the nozzle exit. In this section, we consider this problem.

5.1. *Synchronized waves along the jet*

By joining each mode of wave elements at neighbouring stations for a specified frequency ω, we can know the change in wavenumber for each synchronized wave along the jet as shown in figure 12 for $We_{\delta_0} = 100$. In figure 12(*b*), only 3D waves with $m = k$ are presented for later use. For an unstable wave, two typical frequencies $\omega\delta_0/U = 1$ and 0.5 are selected for illustration. The direction of energy transfer in each capillary wave is indicated by an arrow. Since the jet surface velocity decreases by moving towards the nozzle, the upstream-propagating capillary wave lengthens its

wavelength. It is found that the upstream-propagating capillary wave of $\omega\delta_0/U = 0.5$ has a wavenumber $k\delta_0 = 4.2$ (2D) and 2.6 (3D) at the nozzle exit. This implies that the wavelength of these neutral waves at the nozzle exit is larger than the shear layer thickness δ_0. The figures do not claim that the synchronized wave expressed by each curve exists everywhere. Since the depicted unstable wave is convectively unstable, it can exist only downstream of the location where it is steadily produced. On the other hand, an upstream-propagating capillary wave can exist upstream of a location and serve as a carrier of the streamwise energy flow W and J defined in figure 5.

Each pair of synchronized unstable and upstream-propagating capillary waves in figure 12 may be associated with each other. As explained before, the unstable wave and the neutral wave have a different surface deformation influence depth. Therefore, they behave independently, except where their wavelengths become equal. The existence of an intersection point (the same wavelength at the same station) of a synchronized capillary wave and an unstable wave curve implies that the two waves are interchangeable at that station because the neutral wave can transfer energy to create or eliminate the unstable wave. Therefore, by searching for such a most upstream intersection point in figure 12, we could find a loop exciting the unstable wave in the newly issued liquid. However, it is found that there exists no intersection point where a neutral wave changes to an unstable wave at $U_s/U > 0$, implying that no convectively unstable wave is produced downstream of the nozzle exit ($U_s > 0$).

Nevertheless, there are an upstream-propagating capillary wave reaching the nozzle exit and an unstable wave leaving the nozzle exit, which have the same frequency. Therefore, a capillary wave of frequency ω can turn into an unstable wave of the same frequency ω at the nozzle exit in the following way. Since the capillary wave cannot penetrate into the nozzle, a standing-wave-like pressure field is generated at the nozzle exit by the successive arrival of the incident capillary wave elements at the nozzle exit. The influence of this pressure field, which has no phase mixing, can penetrate deeper from the jet surface and disturbs the shear layer of the newly issued liquid, which has a large velocity U at its edge. Then, a long wave ($\lambda = 2\pi U/\omega$) is produced in response to the frequency ω of the disturbing pressure. This situation is similar to the tripping wire in a classical experiment in which a wall boundary layer unstable wave is excited by a tripping wire placed on the wall. In the framework of local stability analysis, such an exact 3D flow structure cannot be described. Instead, it is described as the production of a synchronized unstable wave at the nozzle exit according to the wave reflection condition (Doppler shift). Since each upstream-propagating capillary wave transfers energy from downstream to upstream, there must be an energy source supporting this capillary wave somewhere downstream. Considering that a real capillary wave hardly propagates upstream against a high-speed surface velocity, the energy source should be located near the nozzle exit where the surface velocity is relatively small. If such a capillary wave is produced by the growth of the unstable wave, this cycle is repeatable and constitutes a self-destabilizing loop in the near-nozzle region.

As described in the next subsection, the linear unstable wave increases its amplitude rapidly from a small, but *unknown* and *not infinitesimal*, initial amplitude ε_0 ($0 < \varepsilon_0 < \delta_0$). As a result, there is a near-nozzle region where the linear unstable wave is largely amplified but its amplitude still remains smaller than δ_0. At these locations, the nonlinear effects neglected in the usual linear stability analysis may serve as a kind of forcing radiating dispersive capillary waves, and result in an upstream-propagating capillary wave that is synchronized with the linear unstable wave and has an amplitude of $O(\varepsilon_0)$. This is a causality discussed in § 3, in that part of the energy transferred

from the baseline flow to the amplified unstable wave is transferred from downstream at a higher fluctuation energy level to upstream at a lower fluctuation energy level. In appendix A, theoretical considerations aiming at supporting this nonlinear upstream-propagating capillary wave production mechanism are provided for reference.

5.2. *Linear spatial growth of unstable waves*

Using the local spatial growth rate, the growth of each synchronized unstable wave along the jet can be calculated by

$$\ln \frac{\varepsilon}{\varepsilon_0} = \int_0^x (-k_i)\,\mathrm{d}x = \int_0^{x/\delta_0} (-k_i\delta_0)\,\mathrm{d}\left(\frac{x}{\delta_0}\right) = 2.4\,Re_{\delta_0} \int_0^{U_s/U} (-k_i\delta_0)\left(\frac{U_s}{U}\right)^2 \mathrm{d}\left(\frac{U_s}{U}\right), \tag{5.1}$$

where (2.3) is used to derive the final expression. The amplification ratio $A = \varepsilon/\varepsilon_0$ is expressed in logarithmic form for later use in § 6. The initial unstable wave amplitude ε_0 denotes the 'apparent' amplitude at the nozzle exit ($x = 0,\ U_s = 0$), extrapolated from the downstream unstable wave growth. To satisfy the boundary condition $\eta(x = 0,\ t) = \partial\eta/\partial t(x = 0,\ t) = 0$, the unstable wave surface deformation in the conventional theory should be expressed as $\eta = 2\varepsilon_0 \sinh(-k_i x)\cos(k_r x - \omega t)$ by introducing the (decaying) wave with negative Reynolds stress contribution. If the unstable wave (5.1) is reproduced by the nozzle exit reflection from the synchronized upstream-propagating capillary wave, the boundary condition is always satisfied automatically.

Figure 13 shows the calculation results of $\ln(\varepsilon/\varepsilon)/Re_\delta$ for the 2D (dashed lines) and 3D (solid lines) waves, from which we can determine the dependence of the amplification ratio $A = \varepsilon/\varepsilon_0$ on $\omega\delta_0/U$ at each station U_s/U for various values of Re_{δ_0}. Each synchronized unstable wave grows at a rate that varies along the jet. As a result, the synchronized unstable wave with the largest amplitude ratio at each station (locally dominant unstable wave) alters depending on the distance from the nozzle exit. It is interesting to note that figure 13 explains the surface deformation pattern changes observed in figure 1 for an equal initial amplitude ε_0. First, a 2D surface deformation emerges, which is then gradually corrugated by the superposition of 3D unstable waves with increased m to form liquid ligaments disintegrating into droplets. The wavelength of the locally dominant 2D unstable is lengthened along the jet.

5.3. *Self-destabilizing loop*

Obviously, the nonlinear capillary wave production region is correlated with the ε_0 value. To gain physical insights into the self-destabilizing loop, we consider a model equation based on the working hypotheses mentioned in § 5.1. The baseline jet flow is forced by the nonlinear unstable wave growth. According to the local linear stability analysis for a vicinity of $x = X$, the amplitude $\mathrm{d}\bar{\eta}_{UPC}(X)/\delta_0$ of the upstream-propagating capillary wave produced by the forcing on an infinitesimal region $(X,\ X + \mathrm{d}X)$ is proportional to the local forcing strength and estimated as $C(\varepsilon_0/\delta_0)^3 A^3(X)\,\mathrm{d}X$ based on the conventional method of regular perturbation expansion in a small parameter $\varepsilon_0/\delta_0 < 1$. The coefficient C is considered to be of $O(1)$ and to depend weakly on X and Re_{δ_0}. For simplicity, we ignore the amplitude variation accompanied by the wavelength variation between the local forcing location and the nozzle exit, i.e. $\mathrm{d}\bar{\eta}_{UPC}(x = 0) = \mathrm{d}\bar{\eta}_{UPC}(x = X)$. A similar synchronized

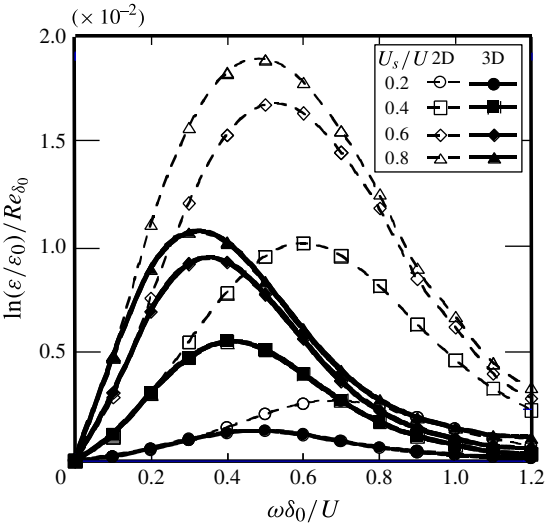

FIGURE 13. Changes in amplitude of 2D and 3D synchronized unstable waves along the jet.

upstream-propagating capillary wave is produced by each local forcing along the jet and superimposed. If such a capillary wave is always produced in phase with the linear unstable wave at each location X, the overlapping capillary waves have the same phase at any upstream location. Therefore, summing up all forcing-produced synchronized capillary waves over an interval $0 \leqslant X \leqslant X_{max} \leqslant \ell_s$, the net amplitude of the synchronized upstream-propagating capillary wave at the nozzle exit is estimated by the following equations (Ξ will be explained after (5.5)):

$$\frac{\bar{\eta}_{UPC}(x=0)}{\delta_0} = \left(\frac{\varepsilon_0}{\delta_0}\right)^3 \int_0^{X_{max}} C\Theta \, \frac{\mathrm{d}X}{\delta_0}, \tag{5.2}$$

$$\Theta = \exp\left[2.4\, Re_{\delta_0} \int_0^{U_s/U} \Xi \left(\frac{U_s}{U}\right)^2 \mathrm{d}\left(\frac{U_s}{U}\right)\right] \quad \text{with} \quad \Xi = 3(-k_i\delta_0) - (\gamma\delta_0). \tag{5.3}$$

The capillary wave amplitude (5.2) produces a new synchronized unstable wave with an initial amplitude $\varphi\bar{\eta}_{UPC}(x=0)$ in the newly issued liquid according to the complete reflection condition. The coefficient φ ($\leqslant 1$) takes a value of $O(1)$ when the upstream transferred energy is all used to produce the new unstable wave. If $\varphi\bar{\eta}_{UPC}(x=0) = \varepsilon_0$, which is possible when

$$\frac{\varepsilon_0}{\delta_0} \sim \left(\frac{\varepsilon_0}{\delta_0}\right)^3 A^3(X = X_{max}) \tag{5.4}$$

in order estimation assuming $\varphi = C = 1$, the upstream-propagating capillary wave and the unstable wave compose a self-destabilizing loop and its initial unstable wave amplitude ε_0/δ_0 is determined as

$$\frac{\varepsilon_0}{\delta_0} = \frac{1}{\sqrt{\varphi}} \frac{1}{\sqrt{2.4\, Re_{\delta_0} \int_0^{U_{s,max}/U} C\Theta \left(\frac{U_s}{U}\right)^2 \mathrm{d}\left(\frac{U_s}{U}\right)}}, \tag{5.5}$$

which must be less than unity. Then, the amplitude $(\varepsilon_0/\delta_0)A$ of the linear unstable wave in the self-destabilizing loop region remains at most $O((\varepsilon_0/\delta_0)^{1/3})$, as can be found from (5.4).

In the inviscid analysis under consideration ($\gamma = 0$ in (5.3)), an upstream-propagating capillary wave, produced at each location, reaches the nozzle exit without amplitude attenuation. We may put $X_{max} = \ell_s$. In this case, ε_0/δ_0 calculated from (5.5) may take a very small value for a large value of Re_{δ_0}. Since such an unstable wave grows in the linear regime extending to a large distance from the nozzle exit, it does not bring about turbulent atomization even at large Re_{δ_0}, consistent with the conventional linear stability analysis, which is based on the assumption of infinitesimal ε_0/δ_0. This prediction is contradictory to experimental observations (e.g. figure 1). Instead, (5.5) implies that an increased ε_0/δ_0 (<1) at larger Re_{δ_0} makes it possible for the linear unstable wave to grow to a nonlinear regime at a location X between X_{max} and ℓ_s, and bring about turbulent atomization downstream. Any contribution from the nonlinear unstable wave evolution is not described by the present analysis. Therefore, for reference, let us consider a self-destabilizing loop operating in the linear region by taking the integral upper limit X_{max} as a location where the linear unstable wave amplitude ε grows to 0.1λ, say, beyond which the unstable wave evolution becomes nonlinear (Li & Umemura 2014). This condition $\varepsilon/\delta_0 = (\varepsilon_0/\delta_0)A(X = X_{max}) = 0.1 \times 2\pi/(k_r\delta_0) \sim 0.4$ combined with (5.4) leads to $\varepsilon_0/\delta_0 \sim [0.1 \times 2\pi/(k_r\delta_0)]^3 \sim 0.064$ and $A = 6.25$. According to (5.1) and (2.3), this implies that, as Re_{δ_0} increases, X_{max} decreases under the condition of almost unchanged ε_0/δ_0. Since the contribution from the nonlinear region will reduce (enlarge) the ε_0/δ_0 (A) value considerably, it is reasonable to assume that ε_0/δ_0 takes a value less than 0.1.

For a given short nozzle, the increased U decreases δ_0. In an asymptotic feature, the jet flow should resemble that of a high-speed orifice jet issued from a large stagnant liquid reservoir. The liquid entering the orifice hole has no short-wave disturbances exciting the jet shear instability. The approach of X_{max} to the nozzle exit beyond a distance will eventually force us to solve the disturbed jet flow field coupled with the nozzle flow to describe a proper self-destabilizing loop, because the pressure wave produced by the successive arrival of capillary wave elements penetrates into the nozzle. A hypothetical scenario derived from this consideration is that, as the jet speed increases, the place where a self-destabilizing loop operates shifts upstream and finally into the nozzle. The 'noise' considered in the conventional linear instability analysis may be interpreted as the disturbances produced by the self-destabilizing loop operating upstream. Then, the atomization onset location could be correlated in terms of nozzle flow Reynolds number in a universal way.

To determine the realizable loop, it is necessary to consider an initial value problem for the baseline jet flow mimicking the laminar jet formation process. The self-destabilizing loop operation for an unstable wave with small $(-k_i)\delta_0$ or $U_{s\ell}$ requires a relatively large initial unstable wave amplitude, which would never be excited in this process. Therefore, the frequency of a realizable unstable wave will be confined to a narrow range.

The above-mentioned behaviour is based on the inviscid analysis. In reality, a viscous effect is not negligible for short waves propagating against large surface velocity. Each upstream-propagating capillary wave attenuates its amplitude and transferred energy exponentially owing to viscous energy dissipation by moving away from the forcing location (i.e. $\mathrm{d}\bar{\eta}_{UPC}(x=0) < \mathrm{d}\bar{\eta}_{UPC}(x=X)$). In (5.3), this modification is expressed by the local spatial damping rate γ, which is derived from the viscous

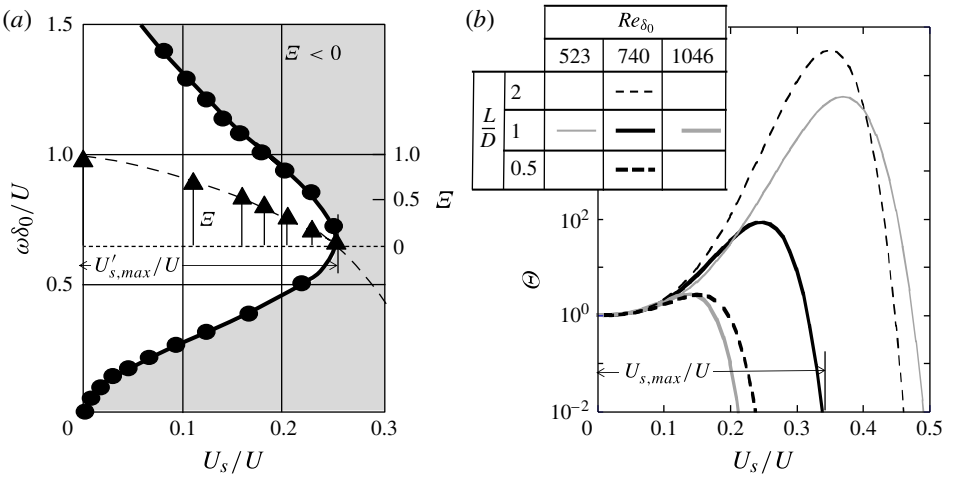

FIGURE 14. Self-destabilizing loop formation region $\Xi > 0$. Here Ξ is calculated for 2D unstable waves in the experimental condition of figure 1. In the grey region, $\Xi < 0$. The triangles express the positive Ξ distribution along the jet for the unstable wave of frequency indicated by the horizontal dashed line.

capillary wave solution of linear spatial evolution analysis for a semi-infinite liquid in a uniform translation of velocity U_s. For a given value of ω, Ξ monotonically decreases from a positive value $\Xi_0(\omega)$ (at $U_s = 0$) to a negative vale. It takes a positive value in the white region ($U_s \leqslant U'_{s,max}(\omega)$) illustrated in figure 14(a). This figure is calculated for a reference jet flow condition ($Re_{\delta_0} = 740$, $L/D = 1$, $We_{\delta_0} = 96.5$). A similar figure is obtained for other jet flow conditions. There is a certain frequency $\omega = \omega_m$ ($\omega_m\delta_0/U \sim 0.6$ in figure 14a) maximizing the value of $U'_{s,max}(\omega)$, for which the Ξ distribution is plotted in figure 14(a). Using this distribution, the Θ distribution defined by (5.3) is calculated as shown by the thick black solid line in figure 14(b). Four other profiles are also drawn to see the effects of L/D and $Re_{\delta 0}$. The thick grey solid line corresponds to the experimental condition of figure 1, roughly. The Θ value rapidly decreases to zero as U_s exceeds $U'_{s,max}$. This implies that the white region characterizes where a self-destabilizing loop may operate. The white region boundary plays a similar role to the integral upper limit $X_{max} = \ell_s$ of the inviscid case, whereas the linear unstable wave can continue to grow until it becomes nonlinear. Therefore, the self-destabilizing loop may be located upstream of the separated nonlinear region and it does not have any contribution from the nonlinear regime. Behaviour other than this is similar to the inviscid case.

Normalizing U_s by $U'_{s,max}$, we find that (5.5) determines ε_0/δ_0 as a function of

$$\frac{X'_{max}}{\delta_0} = 0.8\,Re_{\delta_0}\left(\frac{U'_{s,max}}{U}\right)^3 \quad \text{or} \quad \frac{X'_{max}}{D} = 0.8K^2\left(\frac{U'_{s,max}}{U}\right)^3\frac{L}{D}. \tag{5.6a,b}$$

The calculation condition for the Ξ distribution depicted in figure 14(a) yields $X'_{max}/\delta_0 = 10.4$ and $X'_{max}/D = 0.127$, which leads to an estimate $\varepsilon_0/\delta_0 = 0.0625$ ($A \sim 30$) by calculating (5.5) under the assumption $C = \phi = 1$. Since an increase in U increases $\gamma\delta_0$ and decreases $U_{s,max}/U$, the value of $U_{s,max}/U$ tends to change with Re_{δ_0} in a reciprocal way until the nozzle flow is coupled with the jet flow.

6. Initiation of atomization

In § 5, we found the possibility that the predominant synchronized unstable waves depicted in figure 12 can be repeatedly reproduced at the nozzle exit through their own self-destabilizing loops as illustrated in figure 2. We now consider 2D unstable waves superimposed by 3D unstable waves. The 3D unstable waves take the form of standing waves in the azimuthal direction for a pair of positive and negative m values so as to avoid phase mixing in the azimuthal surface deformation. A precursor of turbulent atomization is the formation of liquid ligaments from the jet surface (see figure 1*a*). Ligament formation is a nonlinear process that generates various new surface waves and prevents the tracing of the subsequent flow development deterministically. This implies that atomizing surface flow eventually becomes turbulent. In this section, using (5.1) we predict where ligaments begin to be formed at given jet speeds. There are several ligament formation mechanisms proposed in the literature.

(i) The action of a gaseous frictional force (Yecko & Zaleski 2005; Shinjo & Umemura 2011) or suction pressure (Taylor 1950) on the bulging surface portion. These possibilities are prohibited in the present model considering the near-nozzle jet surface that is effectively free from gaseous forces. As pointed out by Wu, Tseng & Faeth (1992) and observed in figure 1(*a*), each ligament near the nozzle exit takes the shape formed by liquid ejecting outwards with the local surface velocity and a normal velocity proportional to the jet speed, suggesting that aerodynamic effects are negligible.

(ii) Turbulent eddy ejection (Wu *et al.* 1992), which cannot apply upstream of the turbulent atomization region.

(iii) Destabilization of capillary waves by the action of large transverse inertial forces on the surface layer liquid, which may occur by the passages of amplified 2D unstable waves. The interaction terms between the streamwise and azimuthal disturbance waves are of higher order in the present perturbation analysis.

All these mechanisms may operate in the turbulent atomization region. As a linear process initiating the turbulent atomization nearest to the nozzle exit, we are interested in the development of synchronized 3D waves that effectively form liquid ligaments. Since a liquid ligament must be formed by liquid concentrating from the surrounding trough surface portion, a large difference between axial and azimuthal wavenumbers is not suitable for ligament formation. In fact, the $m = k_r$ unstable wave is a preferential surface deformation pattern that creates liquid surface spikes with minimum surface energy addition (Lyngshansen & Alstrøm 1997). Therefore, in the following we only treat the $m = k_r$ unstable waves as 3D unstable waves.

6.1. *Location of ligament formation onset*

The growth of 3D unstable waves leads to the formation of ligaments that disintegrate into droplets. The self-destabilizing loop fixes the onset location of ligament formation, which may be predicted using the linear 3D unstable wave solution as described below.

Since $\ln(\varepsilon/\varepsilon_0)$ is proportional to Re_δ (see (5.1) and figure 13), the location where amplification enters a nonlinear regime depends crucially on the value of Re_{δ_0}. When the amplitude ε of the locally dominant 3D unstable wave exceeds a fraction ϕ of the wavelength, i.e. $\varepsilon > \phi(2\pi/m)$, the nonlinear effect becomes significant in the formation of a liquid ligament and suppresses the surface deformation (Lyngshansen

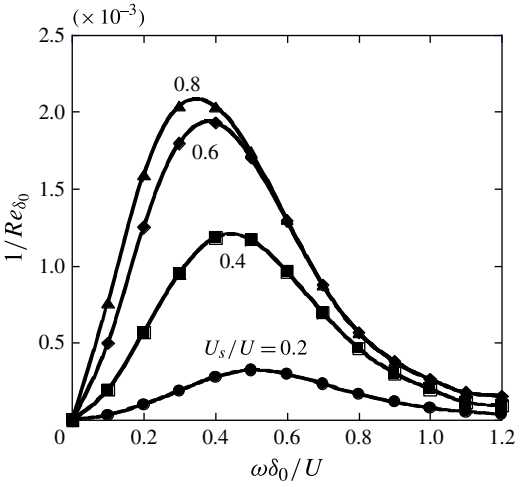

FIGURE 15. Relationships between Re_{δ_0}, $\omega\delta_0/U$ and U_s/U at the instant when 3D unstable waves begin to form ligaments.

& Alstrøm 1997) from an exponential growth to a linear growth. Then, the most upstream location where the condition

$$\ln\frac{\varepsilon}{\varepsilon_0} = \ln\left(\frac{2\pi}{m\delta_0}F\right), \quad F = \frac{\phi}{\varepsilon_0/\delta_0}, \tag{6.1}$$

is satisfied may be defined as the onset location of ligament formation. For reference, we simply assume $F = 10$ for any ω and Re_{δ_0} ranges of interest, based on the suggestion $\phi \sim O(0.1)$ and $\varepsilon_0/\delta_0 \sim O(0.01)$ in § 5. Then, (6.1) can be calculated using the $m\delta_0$ value determined as a function of U_s/U and $\omega\delta_0/U$ in figure 11. It is notable that the choice of the F value does not crucially affect the value of the logarithmic (6.1).

It is convenient to rewrite (5.1) as

$$\frac{1}{Re_{\delta_0}} = \frac{2.4}{\ln\dfrac{\varepsilon}{\varepsilon_0}}\int_0^{U_s/U}(-k_i\delta_0)\left(\frac{U_s}{U}\right)^2 \mathrm{d}\left(\frac{U_s}{U}\right). \tag{6.2}$$

The right-hand side then becomes a function of $\omega\delta_0/U$ for each given U_s/U value. Figure 15 shows this graph for the 3D unstable wave, which has a maximum value at a certain value of $\omega\delta_0/U$ for various U_s/U. The maximum total amplification ratio is achieved at the location $U_s/U \sim 0.8$ for $\omega\delta/U \sim 0.4$. Therefore, turbulent atomization should begin upstream of the location $U_s/U = 0.8$. The peak value at each U_s/U expresses the inverse of the Reynolds number Re_{δ_0}, for which ligament formation is initiated at the U_s/U location under consideration. Thus, we can express the ligament formation onset location U_s/U as a function of Re_{δ_0}.

6.2. *Comparison with experiments*

For experimental comparison, it is more convenient to express the ligament formation onset location x_t/D as a function of $Re_D = UD/\nu$. This can be done using (2.1) and

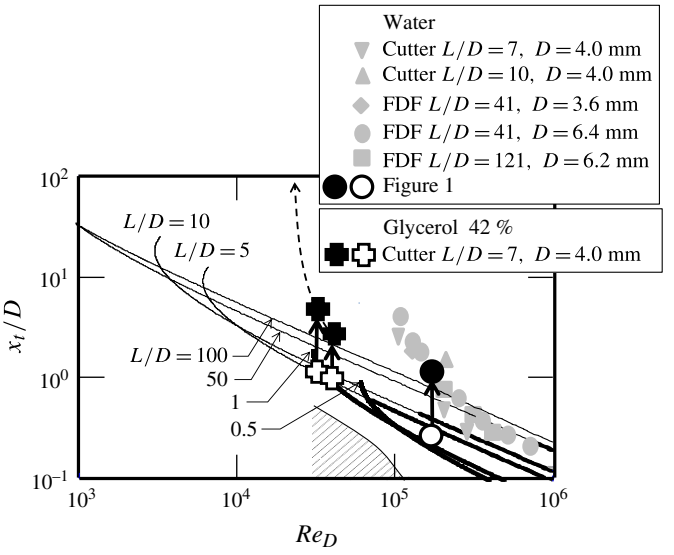

FIGURE 16. Predicted onset location x_t of ligament formation (thin solid lines) in comparison with experiments by Hoyt & Taylor (1977), Taylor & Hoyt (1983) and Wu *et al.* (1995). The thickened line portion satisfies the assumptions made in the present analysis. The open and solid symbols denote the onset location of ligament formation and turbulent atomization, respectively. The hatched region shows the region within which a self-destabilizing loop may operate for the atomizing jet issued from an $L/D=1$ nozzle.

the relationship between Re_{δ_0} and Re_D:

$$Re_{\delta_0} = K\sqrt{\frac{L}{D}}\sqrt{Re_D}. \tag{6.3}$$

The thin (thick at large Re_D) solid lines (called 'L/D curve') in figure 16 show the results of this calculation for water jets. The nozzle length-to-diameter ratio L/D, which represents δ_0/D by (2.1), is taken as a parameter to express the dependence of x_t/D on Re_D for laminar jets issued from various short nozzles. The difference from the assumed value $F=10$ can be counted by slightly translating the L/D curves to the right up ($F>10$) or left down ($F<10$). At Re_D smaller than a critical value specified by the left end of each L/D curve, ligaments are not formed by the instability under consideration. Therefore, a larger value of Re_D is necessary to produce ligaments for a shorter nozzle.

The range of Re_D for which the present analysis is valid is restricted by the following two tradeoff conditions imposed on the shear layer thickness δ_0.

(*a*) The planar shear layer approximation is valid for small δ_0. The surface deformation influence attenuates at a depth of $1/m$ from the baseline jet surface, $y=0$. Curvature effects of the shear flow layer enclosing the jet core may be neglected if $1/m$ is smaller than approximately 5 % of the jet radius, i.e. $2/mD=(2\delta_0/D)/(m\delta_0)<0.05$. Thus, we have the condition

$$Re_D > \left(\frac{40K}{m\delta_0}\right)^2 \frac{L}{D} = 1600K^2\frac{L}{D} \tag{6.4}$$

for a representative unstable wave of $m\delta_0 \sim 1$.

(*b*) The present jet instability is valid for large Weber number $We_{\delta_0} > We_{\delta_0,min} = 100$, i.e.

$$Re_D > \left(\frac{We_{\delta_0,min}}{K}\frac{\sigma D}{\rho\nu^2}\right)^{2/3}\left(\frac{D}{L}\right)^{1/3}. \tag{6.5}$$

This condition indicates that the critical ligament formation Reynolds number depends on the Ohnesorge number as well as L/D.

The thick line portion of each L/D curve in figure 16 expresses the range that satisfies the conditions (6.4) and (6.5) for water.

Figure 16 shows that the leading edge of the turbulent atomization region approaches the nozzle exit as Re_D increases. For short nozzles, x_t/D decreases in inverse proportion to Re_D as a result of the velocity profile relation along the shear layer whose thickness decreases with increasing Re_D. This behaviour is consistent with experimental observations as described below.

A quantitative comparison with experiment is difficult because there are few reports detailing jet surface deformation. Here we consider the experimental results of Hoyt & Taylor (1977), Taylor & Hoyt (1983) and Wu *et al.* (1995). In these experiments, the nozzle exit velocity profile has not been measured, so that the actual value of δ_0 is unknown. A close look at the surface deformation in figure 1(*a*) reveals the presence of a superimposed 3D unstable wave from immediately downstream of the nozzle exit.

In figure 16, the onset locations of ligament formation and atomization, taken from figure 1(*a*), are plotted as the open and solid circles, respectively. As mentioned before, the ligament formation onset location x may be defined as the location where the surface deformation amplitude begins to increase linearly along the jet in the photograph. The open circle in figure 16 expresses this location, which is on the thickened $L/D=2$ curve. According to (5.6), this location $x_t/D \sim 0.25$ corresponds to $U_s/U \sim 0.327$ $(L/D=1)$ or 0.227 $(L/D=3)$.

The nozzle used in the experiment has a straight tube with a unit length-to-diameter ratio followed by a convergent nozzle portion. For comparison, this nozzle should be replaced by an equivalent straight nozzle of apparent length L, which yields the real (but unknown) value of δ_0 by (2.1). The value of δ_0 was estimated as follows. The wavelength λ of the dominant 2D unstable wave visible near the nozzle exit in figure 1(*a*) was measured to obtain the evaluation $\lambda/D = 0.0551$. Assuming that this unstable wave has the wavenumber $k\delta_0 = 1.5$ of the 2D unstable wave dominant near the nozzle exit, we obtain the expression $\delta_0/D = 1.5\lambda/(2\pi D) = 0.0131$, which leads to $L/D = (0.0131/K)^2 Re_D = 3.09$. Although this value is different from the value of L/D (approximately 2) where the open circle is located, it may be reasonable to say that agreement is fairly good, at least in order of magnitude, even if the uncertainties involved in the logarithmic factor $\ln(\varepsilon/\varepsilon_0)$ are taken into account.

Figure 17 shows photographs from the experiments of Wu *et al.* (1995), from which we may measure the atomization onset location. The figure also illustrates the experimental methods; two types of experiment are conducted for jets issued from the convergent nozzles. In the type A experiments, the convergent nozzle is connected to a straight nozzle of length L. In the type B experiments, a cutter with a straight hole of length L is set apart from the convergent nozzle. Wu *et al.* measured the dependence of the atomization onset location on jet speed, using pulsed shadowgraph photography, as shown in figure 17. The experimental uncertainties (95 % confidence) of this determination were less than 40 %. The water jet data, including the turbulent jet case with large L/D, are plotted with grey solid symbols in figure 16. Obviously,

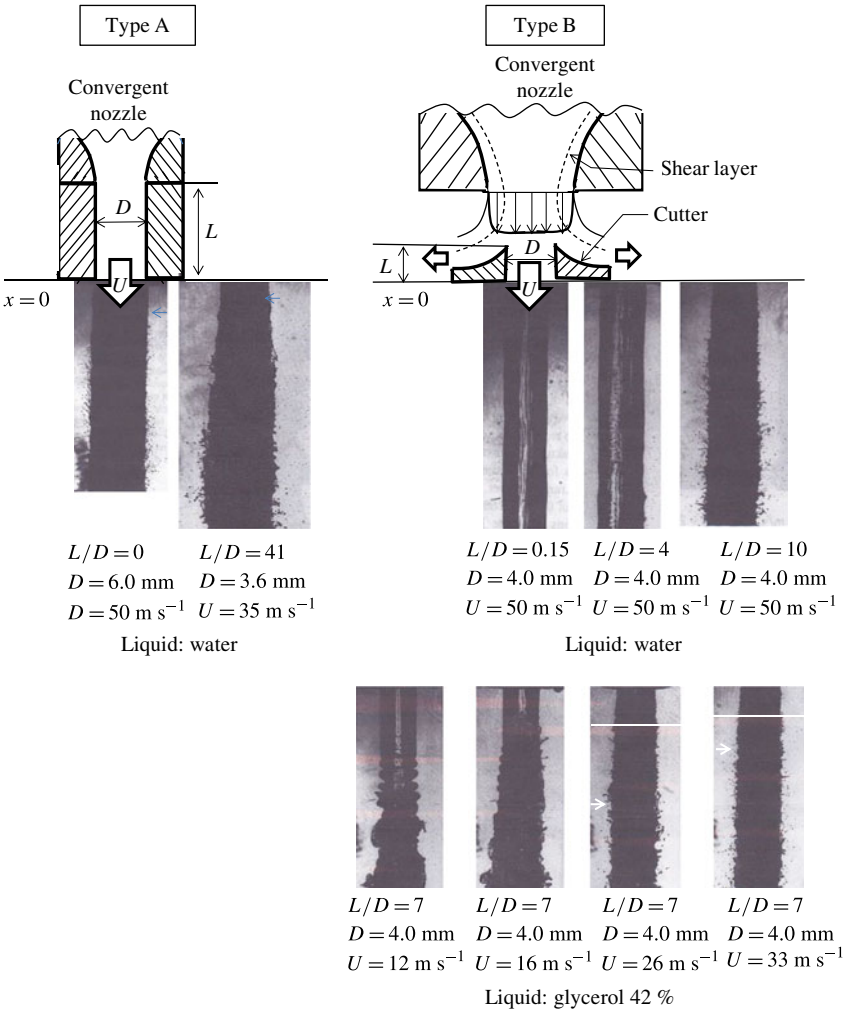

FIGURE 17. Backlit photographs obtained in Wu *et al.* (1995)'s experiments. The contraction ratio of the convergent nozzle portion is roughly 100. Type A has a constant-diameter passage connected with the convergent nozzle. Type B has a cutter with a constant-diameter passage downstream of the convergent nozzle exit.

the corresponding onset locations of ligament formation must be located upstream of these points.

The existence of liquid kinematic viscosity is essential for the formation of δ_0 in the nozzle flow. To examine the validity of condition (6.5) for the excitation of the liquid shear layer flow instability, the four photographs in figure 17, taken for 42 % glycerol jets issued from the cutter with $L/D = 7$ and $D = 4$ mm, were used to measure the atomization onset locations plotted as solid crosses in figure 16. Compared to water, 42 % glycerol has almost the same density but a smaller surface tension coefficient and significantly larger kinematic viscosity (lager Ohnesorge number). As a result, the region satisfying both (6.4) and (6.5) for 42 % glycerol is extended from that for water to the smaller Re_D side. The following are also notable. As explained in § 6.3, an effective L/D value for a short cutter jet is considered to take a considerably smaller

value than the cutter aspect ratio ($L/D = 7$). In the 42 % glycerol jet photographs, the location x_t specified by the $L/D = 1$ curve at the corresponding Re_D value in figure 16 is indicated by a white horizontal line for reference. It is observed that (i) the surface deformation amplitude begins to increase linearly from a location near this line, and (ii) the $L/D = 2$ curve yields the critical ligament formation Reynolds number consistent with the $U = 16$ m s^{-1} experiment.

The boundary of the hatched region in figure 16 shows the location $U_{s,max}/U$ indicated in figure 14(*b*) for laminar $L/D = 1$ jets, upstream of which a self-destabilizing loop may operate. For a jet of $L/D > 1$, this boundary shifts upwards in the figure by L/D times. Consistent with our prediction, the figure indicates that the self-destabilizing loop of the atomizing short nozzle jet is located upstream of the ligament formation onset location. At a large Reynolds number, a self-destabilizing loop determining the atomization onset location is considered to move into the nozzle flow. On the other hand, in the 42 % glycerol jet photograph of $U = 12$ m s^{-1}, we can observe a significant surface deformation growth without atomization, implying that the unstable wave of small ε_0/δ_0 is produced by a self-destabilizing loop within the hatched region in figure 16.

The plots for the 42 % glycerol jets suggest that the change in ligament formation onset location with Re_D is more moderate than that for the atomization onset location. The two onset locations approach each other at larger Re_D. This trend should be the same for the water jets. Therefore, the data of Wu *et al.* (1995) suggest that the ligament formation onset occurs close to the atomization onset location at large Re_D. In fact, since δ_0/D decreases with increasing Re_D, the two onset locations should approach each other. In this respect, we should note that figure 16 is expressed on a logarithmic scale, which increases the resolution at small x, while the rapid and fine surface deformation near the nozzle exit becomes difficult to observe with high resolution. Therefore, a strict comparison in figure 16 is meaningless at large Re_D. When expressed on a linear scale, all the curves in figure 16 collapse to a single line approaching the abscissa. Hence, in the present comparison with experiment, it only matters whether the atomization onset location measured in the experiments exhibits a similar trend to the thick L/D curves. The data of Wu *et al.* have coincident trends with the thick L/D curves, which do support the claim of Wu *et al.* that jet surface deformation is scaled by the shear layer thickness δ_0. It is also worth mentioning that the mean size of atomized droplets is correlated with the wavelength of the locally dominant 3D unstable wave, $\lambda = [2\pi(c_r/U)/(\omega\delta_0/U)]\delta_0$, implying that, consistent with Wu *et al.*'s non-turbulent jet experiments, the droplet size is scaled by δ_0 (the value of c_r/U for 3D unstable waves is nearly unity at any U_s/U).

6.3. *Laminarization by flow separation from nozzle inlet edge*

The cutter in the experiments of Wu *et al.* (1995) is used to produce a uniform stream flowing into a straight hole by discarding the boundary layer flow portion formed by the convergent nozzle wall. Thus, its ideal function would be to create a nozzle flow consistent with the present analysis. However, the experimental results indicate that this is not achieved, because (i) a jet without significant surface deformation is issued from the cutter with $L/D < 7$ (see the photographs for $L/D = 0.16$ and 4 in figure 17), while (ii) the jet directly issued at the same Re_D from the convergent nozzle ($L/D = 0$) exhibits turbulent atomization near the nozzle exit as seen in figure 17. These two pieces of evidence clearly indicate that the turbulent atomization of (ii) is caused by the presence of a thin liquid shear layer.

The present analysis provides an answer to the question raised by (i), if the core flow issued from the convergent nozzle has an inward velocity at the leading edge of the cutter and forms an open cavity between the liquid flow and the hole wall. In fact, we assume that the flow within the cutter hole develops a boundary layer flow according to (2.1). The values $L/D = 0.15$, $D = 4$ mm and $Re_D = 2 \times 10^5$ then yield $\delta_0/D = 0.00261$ and $We_{\delta_0} = 361$. The Weber number is large enough to excite the shear layer flow instability, but the thickness of the shear layer produced by the leading edge of the cutter is so thin that the velocity profile relaxes within the hole. The subsequent jet flow cannot but be subject to an aerodynamic instability similar to figure 1(*b*). Thus, we observe a laminar jet issuing from the cutter. This is a similar phenomenon as observed by Arai *et al.* (1985). They found that a turbulent atomizing water jet issued from a straight nozzle with a sharp-edged inlet connected to a larger-diameter tube changes to a smooth surface jet when the nozzle flow experiences a super-cavitation state at a larger jet speed. Therefore, for $L/D < 7$, for which a laminar jet is observed, the inlet flow of the cutter hole separates from the leading edge without reattachment. As the cutter length is increased further, the separated flow reattaches to the hole wall and the cutter comes to function as expected.

6.4. *Turbulent jet atomization features implied from the present model*

In figure 16, the atomization onset locations for turbulent jets are also plotted. The cutter hole length $L/D = 41$ at $Re_D \sim 10^5$ is very short compared to the so-called inlet length L_i for fully developed laminar pipe flow ($L_i/D = 0.065Re_D$), and close to the upper limit of the inlet length for fully developed turbulent pipe flow ($L_i/D = 25$–40). Since the grey solid squares for $L/D = 121$ are located at similar places as the grey solid circles for $L/D = 41$ in figure 17, we infer that the plots for $L/D = 41$ show turbulent jet properties. Interestingly, the turbulent jets exhibit a similar behaviour to a laminar jet for small L/D. Considering the laminar sublayer and logarithmic layer in the turbulent nozzle flow and the turbulent atomization maintenance by a surface flow instability supported by the Reynolds stress, the initiation of turbulent atomization in the turbulent jets might also be explained using the present analysis by choosing the shear layer thickness appropriately. In a convergent nozzle, in which there is a pressure decrease in the direction of flow, the fluid accelerates and the boundary layer becomes thinner. The accelerating fluid maintains the fluid close to the wall in motion. When we consider the average flow, the turbulent transition in a straight long hole plays a similar role to the convergent nozzle, because the turbulent eddies impart a high flow in the vicinity of the wall and tend to make the average flow uniform over the cross-section. This means that the average shear flow region is confined to a thin layer on the wall. The instability of this average shear flow has the same characteristics as explored in the present analysis, because the Reynolds stress supplies energy to deform the jet surface. If this shear layer flow instability is dominant near the nozzle exit, it is not surprising that the turbulent jet results in the same atomization onset location as the laminar jet case.

Wu *et al.* (1995) showed that the turbulent atomization onset locations are correlated in terms of the Weber number based on the nozzle diameter ($\rho U^2 D/\sigma$). This result is understandable, if we consider that the ratio of the effective δ_0 to the nozzle diameter falls in a restricted range for all cases and that the atomization phenomena are scaled by δ_0. Since the magnitude of turbulent disturbance is much larger than that contained in the laminar nozzle flow, the above evidence suggests that the main mechanism

initiating turbulent atomization near the nozzle exit is the disturbance associated with the downstream phenomena. Hence, we infer that the surface deformation immediately downstream of the nozzle exit may be described within the framework of a linear stability analysis. The only difference between laminar and turbulent nozzle flow is what produces unstable waves in the laminar shear flow layer. In the case of a laminar jet, there are no disturbances contained in the high-speed laminar stream. The upstream-propagating capillary waves disturb the shear layer from the outer side and produce synchronized unstable waves in the shear layer. For a turbulent jet, the shear layer is disturbed from the inner side by the high-speed turbulent stream. Nevertheless, the upstream-propagating capillary waves still may take part in the production of unstable waves.

Finally, we discuss the possibility of ligament formation by a two-stage instability (Faraday 1831; Kelvin 1871; Rayleigh 1883; Taylor 1950; Benjamin & Ursell 1954; Villermaux & Clanet 2002) in the turbulent atomization region. The surface liquid at a station is displaced transversely by the passage of dominant 2D unstable wave elements (wavenumber k_r, phase speed c_r) at a frequency $\Omega = k_r(c_r - U_s)$. Therefore, if there is a 3D surface deformation with large wavenumber m resonant with this oscillation, e.g. $\omega = \sqrt{\sigma m^3/\rho} = 2\Omega$, the surface deformation is destabilized to form ligaments when the dimensionless displacement amplitude $m\varepsilon$ is large enough. Figure 12 indicates that such a capillary wave is not excited naturally. However, once the 3D unstable wave experiences nonlinear growth, higher-order capillary waves are generated by nonlinearities. Therefore, this two-stage instability may operate in the turbulent atomization region. The turbulent atomization will then become similar to ultrasonic atomization (Wood & Loomis 1927; Lang 1962; Goodridge, Shi & Lathrop 1996; Goodridge, Hentschel & Lathrop 1999).

7. Conclusion

To realize steadily unstable flow in a jet, there must be a deterministic mechanism to reproduce the same unstable waves at a fixed location. In the present study, the fluid dynamical structure initiating steady turbulent atomization was theoretically examined for high-speed laminar water jets issuing from a short nozzle into stagnant air. It was found from the linear stability analysis of the local baseline jet flow that the liquid shear layer produced during the nozzle passage can bring about the steady onset of turbulent atomization without any influence of the surrounding gas flow, by virtue of the following self-destabilizing mechanism operating near the nozzle exit.

The key point is that the liquid shear flow with a high velocity gradient produces strong unstable waves near the nozzle exit where the surface velocity takes small values. It was shown from a consideration of higher-order solution behaviour that, at large Re_δ, the growth of a linear unstable wave along the jet produces a synchronized capillary wave propagating upstream even in the linear regime. Therefore, the development of unstable waves near the nozzle exit, caused by energy transfer from the baseline jet flow, produces upstream-propagating waves that transport energy upstream to reproduce the same unstable waves in the newly issued liquid at the nozzle exit. Thus, this cycle is repeatable. The growth of self-destabilizing 2D and 3D unstable waves describes the development of axisymmetric surface deformation followed by the development of 3D unstable waves that initiate turbulent atomization. The predicted onset location of ligament formation is consistent with experimental observations including turbulent jets.

Acknowledgements

The present study was supported by a Grant-in-Aid for Scientific Research from the Ministry of Education, Culture, Sports, Science and Technology of Japan and by the 'Ground-based Research Program for Space Utilization' promoted by the Japan Space Forum.

Appendix A. Origin of upstream-propagating capillary wave

A local stability analysis based on the parallel flow approximation is not applicable in the near-nozzle region, because the baseline flow varies significantly in the axial direction. An accurate analysis may be performed in a framework of global mode analysis (e.g. Chomaz 2005) accounting for nonlinearity and possible coupling with the nozzle flow. Nevertheless, it would be instructive to use the present local stability solutions to gain insights. Various processes may produce upstream-propagating dispersive capillary waves. In the present study, we focused on dispersive capillary waves produced by the unstable wave growth described by (5.1), because the nonlinear term effects neglected in the linear theory may become significant downstream.

The considered unstable shear flow field should be a function of dimensionless initial unstable wave amplitude ε_0/δ_0, whose value is assumed to be less than unity but unknown. The usual linear stability analysis solves the eigenvalue problem posed by the first-order homogeneous equation system in a hierarchy of regular perturbation equation systems generated for the temporally periodic flow field expanded into a power series of ε_0/δ_0. In view of figure 1, it is obvious that ε_0/δ_0 is not infinitesimal. Therefore, to characterize the present jet instability to $O(\varepsilon_0/\delta_0)$, we need to consider nonlinear effects described by the higher-order equations as well.

In the present local stability analysis, it is assumed that such perturbation equation systems hold locally for the parallel flow in a vicinity of each location $x = X$ as long as $\varepsilon_0 A(X)/\delta_0 < 1$ and all flow variables appearing in them are smoothly continuous along the jet. Equation (5.1) indicates that a dominant unstable wave grows rapidly due to a large value of Re_{δ_0} and saturates at a neutralizing location $x = \ell_s$. Therefore, higher-order contributions resulting from a dominant unstable wave growth were examined by retaining those inhomogeneous terms associated with (5.1) only. The linear unstable wave used for this analysis has a 2D surface deformation $\eta/\delta_0 = (\varepsilon_0/\delta_0)A\,\mathrm{e}^{\mathrm{i}(\alpha\xi-\omega t)} + \mathrm{c.c.}$ of a specific frequency ω ($\geqslant 0$), where $\xi = x - X$ and $A = \mathrm{e}^{\beta X}$. To distinguish from the general wavenumber k of Fourier transformation used later, the wavenumber and growth rate of the considered linear unstable wave are denoted by α and β, respectively; A takes a large value away from the nozzle exit. It should be noted that, in the vicinity of each location $x = X$ belonging to a linear region where $\varepsilon_X/\delta_0 \equiv (\varepsilon_0/\delta_0)A(x = X) < 1$, ε_X/δ_0 plays the same role as the expansion parameter ε_0/δ_0 in the local perturbation equation systems treated in the following analysis.

In the vicinity of $x = X$, the second-order equation system yields particular solutions that depend on time t and local axial coordinate ξ through the factors $A^2\,\mathrm{e}^{2\beta\xi}\mathrm{e}^{2\mathrm{i}(\alpha\xi-\omega t)}$, $A^2\,\mathrm{e}^{2\beta\xi}$ and their complex conjugates. These solutions are multiplied by the linear unstable wave solution to produce the inhomogeneous terms appearing in the third-order equation system, which depend on t and ξ through the factors $A^3\,\mathrm{e}^{3\beta\xi}\mathrm{e}^{\mathrm{i}(\alpha\xi-\omega t)}$ and its complex conjugate in particular. Therefore, the third-order equation system for the temporally harmonic flow field takes the same form as the first-order equation system, except for the given temporally harmonic inhomogeneous

terms, which may be regarded as an 'external force distribution' acting on the baseline jet flow. This third-order equation system yields a particular solution synchronized with the linear unstable wave. As a result, the perturbation equations, which govern the temporally harmonic disturbances valid to the third order, may be reduced to a single equation governing the temporally harmonic surface deformation η/δ_0 in the form $\mathscr{D}[-\mathrm{i}\,\partial/\partial\xi;\,\omega]\eta\,\mathrm{e}^{-\mathrm{i}\omega t} = S(X)\,\mathrm{e}^{(3\beta+\mathrm{i}\alpha)\xi}\mathrm{e}^{-\mathrm{i}\omega t}$, where $\mathscr{D}$ expresses the functional form of the dispersion relation derived from the local linear stability analysis (Huerre & Monkewitz 1990) and $S = (\varepsilon_0/\delta_0)^3A^3(X)B(X)$ (see appendix B). Here B is a quantity of $O(1)$. Note that, unlike the usual linear stability analysis, we are now considering the $O(\varepsilon_0/\delta_0)$ equation with the forcing caused by the nonlinear unstable wave growth effects. What we would like to know is the effect of the forcing applied to an infinitesimal vicinity of $x = X$, i.e. $0 \leqslant \xi \leqslant \mathrm{d}X$, say. Therefore, the forcing is considered to vanish outside of this region. The Green's function formalism of this problem is facilitated by considering the Fourier-transformed equation in the framework of local instability analysis. We obtain the Fourier-transform solution $\mathrm{d}\eta_k = (2\pi)^{-1/2}S(X)\,\mathrm{d}X/\mathscr{D}(k,\omega)$. Its inverse transformation results in a synchronized upstream-propagating capillary wave of amplitude $\mathrm{d}\bar{\eta}_{UPC} = (\varepsilon_0/\delta_0)^3A^3C\,\mathrm{d}X$ upstream of the forcing portion, in particular, at $x = X - 0$, where $C = |B(X)R(X)|$. Here R is the residual $R = 1/[\mathrm{d}\mathscr{D}/\mathrm{d}k\ (k = -k';\,\omega)]$ of the pole $k = -k'(\omega)$ expressing the upstream-propagating capillary wave of the local dispersion relation. Therefore, the resulting wave coincides with the upstream-propagating capillary wave presented in § 4. This result indicates that the first-order equation system to be treated in the present linear stability analysis should have the inhomogeneous terms appearing in the third-order equation system, so that the $O(\varepsilon_0/\delta_0)$ upstream-propagating capillary wave produced by the nonlinear unstable wave growth at locations apart from the nozzle exit might be captured.

The following should be noted. When we consider the wave produced upstream of $x = X$ by the local forcing on an infinitesimal region $[X,\ X + \mathrm{d}X]$, the formal $O(\varepsilon_0/\delta_0)$ equation derived above is similar to that used in the absolute or convective instability analysis. The difference is only that, instead of an impulsive forcing in space and time, a temporally periodically changing force distribution is considered to act on an infinitesimal interval $\mathrm{d}X$ about $x = X$. Part of the energy introduced by a forcing is transferred in the upstream direction as a dispersive capillary wave. For the periodic forcing under consideration, the dispersive capillary waves take the form of an upstream-propagating capillary wave synchronized with the given unstable wave. A similar upstream-propagating capillary wave is producible at any location X where the linear unstable wave amplitude ε_0A is smaller than δ_0. According to the local stability analysis concept, there must be a synchronized upstream-propagating capillary wave, shown in figure 12, which is connected with the forcing-produced synchronized capillary wave so as to conserve the upstream transferred energy along the jet. This explains the origin of a synchronized upstream-propagating capillary wave expressed by figure 12.

Appendix B. Derivation of governing equation for surface deformation

The perturbation equation system treated within the local stability analysis framework is considered for the temporally harmonic, disturbed flow field $(\eta, u', v', p') = [\Delta(\xi),\ U(\xi, y),\ V(\xi, y),\ P(\xi, y)]\,\mathrm{e}^{-\mathrm{i}\omega t}$ valid to order $O((\varepsilon_X/\delta_0)^3)$ where $\varepsilon_X/\delta_0 = (\varepsilon_0/\delta_0)A(x = X) < 1$. Some equations have, on their right-hand sides, an inhomogeneous term associated with the linear unstable wave growth in a vicinity of $x = X$, which

takes a form such as $(\varepsilon_0/\delta_0)^3 A^3 F(y)\,\mathrm{e}^{(3\beta+\mathrm{i}\alpha)\xi-\mathrm{i}\omega t}$ at $0\leqslant\xi\leqslant \mathrm{d}X$ and vanishes elsewhere. Denoting the Fourier components of Δ, U, V and P by Δ_k, U_k, V_k and P_k, respectively, the Fourier-transformed ($(2\pi)^{-1/2}\int_{-\infty}^{+\infty}\mathrm{d}\xi\,\mathrm{e}^{-\mathrm{i}k\xi}$ operated) equations are expressed as follows:

$$\mathrm{i}kU_k+\frac{\mathrm{d}V_k}{\mathrm{d}y}=0, \tag{B 1}$$

$$\mathrm{i}(ku-\omega)U_k+V_k\frac{\mathrm{d}u}{\mathrm{d}y}+\frac{1}{\rho}\mathrm{i}kP_k=\left(\frac{\varepsilon_0}{\delta_0}\right)^3 A^3F_u\frac{1}{\sqrt{2\pi}}\frac{\mathrm{e}^{(3\beta+\mathrm{i}\alpha+\mathrm{i}k)\mathrm{d}X}-1}{3\beta+\mathrm{i}\alpha+\mathrm{i}k}$$
$$=\frac{1}{\sqrt{2\pi}}\left(\frac{\varepsilon_0}{\delta_0}\right)^3 A^3F_u\mathrm{d}X, \tag{B 2}$$

$$\mathrm{i}(ku-\omega)V_k+\frac{1}{\rho}\frac{\mathrm{d}P_k}{\mathrm{d}y}=\frac{1}{\sqrt{2\pi}}\left(\frac{\varepsilon_0}{\delta_0}\right)^3 A^3F_v\,\mathrm{d}X, \tag{B 3}$$

subject to

$$V_k(0)-\mathrm{i}[kU_s-\omega]\Delta_k=\frac{1}{\sqrt{2\pi}}\left(\frac{\varepsilon_0}{\delta_0}\right)^3 A^3G\,\mathrm{d}X, \tag{B 4}$$

$$P_k(0)-\sigma k^2\Delta_k=\frac{1}{\sqrt{2\pi}}\left(\frac{\varepsilon_0}{\delta_0}\right)^3 A^3H\,\mathrm{d}X, \tag{B 5}$$

$$P_k(\infty)=U_k(\infty)=V_k(\infty)=0. \tag{B 6}$$

Note that F_u, F_v, G and H are independent of k; and that $F_u(y)$ and $F_v(y)$ vanish at $y=\infty$.

From (B 3) and (B 2), we obtain

$$V_k=\frac{1}{\mathrm{i}(ku-\omega)}\left[-\frac{1}{\rho}\frac{\mathrm{d}P_k}{\mathrm{d}y}+\frac{1}{\sqrt{2\pi}}\left(\frac{\varepsilon_0}{\delta_0}\right)^3 A^3F_v\,\mathrm{d}X\right], \tag{B 7}$$

$$U_k=\frac{1}{\mathrm{i}(ku-\omega)}\left[\frac{1}{\mathrm{i}\rho(ku-\omega)}\frac{\mathrm{d}u}{\mathrm{d}y}\frac{\mathrm{d}P_k}{\mathrm{d}y}-\frac{1}{\rho}\mathrm{i}kP_k\right.$$
$$\left.+\left\{-\frac{1}{\mathrm{i}(ku-\omega)}\frac{\mathrm{d}u}{\mathrm{d}y}F_v+F_u\right\}\frac{1}{\sqrt{2\pi}}\left(\frac{\varepsilon_0}{\delta_0}\right)^3 A^3\,\mathrm{d}X\right]. \tag{B 8}$$

Substituting these into (B 1), we obtain the governing equation for P_k as

$$\frac{\mathrm{d}^2P_k}{\mathrm{d}y^2}-2\frac{k\dfrac{\mathrm{d}u}{\mathrm{d}y}}{ku-\omega}\frac{\mathrm{d}P_k}{\mathrm{d}y}-k^2P_k=\left[\rho\mathrm{i}kF_u+\rho\frac{\mathrm{d}G_v}{\mathrm{d}y}-2k\frac{\mathrm{d}u}{\mathrm{d}y}\frac{\rho G_v}{ku-\omega}\right]\frac{1}{\sqrt{2\pi}}\left(\frac{\varepsilon_0}{\delta_0}\right)^3 A^3\,\mathrm{d}X. \tag{B 9}$$

Equation (B 4) combined with (B 7) leads to

$$\frac{\mathrm{d}P_k}{\mathrm{d}y}(0)=\rho(kU_s-\omega)^2\Delta_k+[-\mathrm{i}(kU_s-\omega)G+\rho F_v(0)]\frac{1}{\sqrt{2\pi}}\left(\frac{\varepsilon_0}{\delta_0}\right)^3 A^3\,\mathrm{d}X. \tag{B 10}$$

Using (B 5) and (B 10), we can integrate (B 9) from $y = 0$ to ∞, and obtain the following form of equation:

$$P_k(\infty) = \mathscr{D}(k, \omega)\Delta_k - \frac{1}{\sqrt{2\pi}}\left(\frac{\varepsilon_0}{\delta_0}\right)^3 A^3 B(\alpha, \beta, \omega)\,\mathrm{d}X = 0. \tag{B 11}$$

In the text, Δ_k is rewritten as $\mathrm{d}\eta_k$ to indicate the contribution from the forcing on the infinitesimal region ($\mathrm{d}X$).

REFERENCES

ARAI, M., SHIMIZU, M. & HIROYASU, H. 1985 Break-up length and spray angle of a high speed liquid jet. In *Proceedings of the 3rd International Conference on Liquid Atomization and Spray Systems*, vol. 1, pp. IB/4/1–IB/4/10.

BATCHELOR, G. K. & GILL, A. E. 1962 Analysis of the stability of axisymmetric jets. *J. Fluid Mech.* **14**, 529–551.

BENJAMIN, T. B. & URSELL, F. 1954 The stability of the plane free surface of a liquid in vertical periodic motion. *Proc. R. Soc. Lond.* A **225**, 505–515.

BRIGGS, R. J. 1964 *Electron–Stream Interaction with Plasmas*. MIT Press.

CHANDRASEKHAR, S. 1961 *Hydrodynamic and Hydromagnetic Stability*. Clarendon.

CHOMAZ, J.-M. 2005 Global instabilities in spatially developing flows: non-normality and nonlinearity. *Annu. Rev. Fluid Mech.* **37**, 357–392.

DAVIES, J. T. & YOUNG-HOON, A. A. 1974 Restrained turbulent jets of a non-Newtonian solution. *Chem. Engng Sci.* **29**, 1115–1121.

EGGERS, J. & VILLERMAUX, E. 2008 Physics of liquid jets. *Rep. Prog. Phys.* **71**, 036601.

ESCH, R. E. 1957 The instability of a shear layer between two parallel streams. *J. Fluid Mech.* **3**, 289–303.

FARADAY, M. 1831 On a peculiar class of acoustical figures; and on certain forms assumed by groups of particles upon vibrating elastic surfaces. *Phil. Trans. R. Soc. Lond.* **52**, 299–318.

FENN, R. W. & MIDDLEMAN, S. 1969 Newtonian jet stability: the role of air resistance. *AIChE J.* **12**, 379–383.

GALLAIRE, F. & CHOMAZ, J.-M. 2004 The role of boundary conditions in a simple model of incipient vortex breakdown. *Phys. Fluids* **16**, 274–286.

GOODRIDGE, C. L., HENTSCHEL, H. & LATHROP, D. P. 1999 Breaking Faraday waves: critical slowing of droplet ejection rates. *Phys. Rev. Lett.* **82**, 3062–3065.

GOODRIDGE, C. L., SHI, W. T. & LATHROP, D. P. 1996 Threshold dynamics of singular gravity–capillary waves. *Phys. Rev. Lett.* **76**, 1824–1827.

GORDILLO, J. M. & PÉREZ-SABORID, M. 2005 Aerodynamic effects in the break-up of liquid jets: on the first wind-induced break-up regime. *J. Fluid Mech.* **541**, 1–20.

GOROKHOVSKI, M. & HERRMANN, M. 2008 Modeling primary atomization. *Annu. Rev. Fluid Mech.* **40**, 343–366.

HOYT, J. W. & TAYLOR, J. J. 1977 Waves on water jets. *J. Fluid Mech.* **88**, 119–123.

HUERRE, P. & MONKEWITZ, P. A. 1990 Local and global instabilities in spatially developing flows. *Annu. Rev. Fluid Mech.* **22**, 473–537.

HUH, K. Y., LEE, E. J. & KOO, J. Y. 1998 Diesel spray atomization model considering nozzle exit turbulence conditions. *Atomiz. Sprays* **8**, 453–469.

INOUE, O. 1985 A new approach to flow problems past a porous plate. *AIAA J.* **23**, 1916–1921.

KARASAWA, T., TANAKA, M., ABE, K., SHIGA, S. & KURABAYASHI, T. 1992 Effect of nozzle configuration on the atomization of a steady spray. *Atomiz. Sprays* **2**, 411–426.

KELVIN, LORD 1871 Hydrokinetic solutions and observations. *Phil. Mag.* **42**, 362–377.

LANG, R. J. 1962 Ultrasonic atomization of liquids. *J. Acoust. Soc. Am.* **34**, 6–8.

LASHERAS, J. C. & HOPFINGER, E. J. 2000 Liquid jet instability and atomization in a coaxial gas stream. *Annu. Rev. Fluid Mech.* **32**, 275–308.

LEVICH, V. G. 1992 *Physicochemical Hydrodynamics*. Prentice-Hall.

LI, Y. & UMEMURA, A. 2014 Two-dimensional numerical investigation on the dynamics of ligament formation by Faraday instability. *Intl J. Multiphase Flow* **60**, 64–75.

LIN, S. P. 2003 *Breakup of Liquid Sheets and Jets*. Cambridge University Press.

LIN, S. P. & REITZ, R. 1998 Drop and spray formation from a liquid jet. *Annu. Rev. Fluid Mech.* **30**, 85–105.

LOVE, A. E. H. 1911 *Some Problems of Geodynamics*. Cambridge University Press.

LYNGSHANSEN, P. & ALSTRØM, P. 1997 Perturbation theory of parametrically driven capillary waves at low viscosity. *J. Fluid Mech.* **351**, 301–344.

MARMOTTAN, P. & VILLERMAUX, E. 2004 On spray formation. *J. Fluid Mech.* **498**, 73–111.

MATTINGLY, G. E. & CHANG, C. C. 1974 Unstable waves on an axi-symmetric jet column. *J. Fluid Mech.* **65**, 541–560.

MAYER, E. 1961 Theory of liquid atomization in high velocity gas stream. *Am. Rocket Soc. J.* **31**, 1783–1785.

MCCARTHY, M. J. & MALLOY, N. A. 1974 Review of stability of liquid jets and the influence of nozzle design. *Chem. Engng J.* **7**, 1–20.

PAPAGEORGIOU, D. T. & SMITH, F. T. 1989 Linear stability of the wake behind a flat plate placed parallel to a uniform stream. *J. Fluid Mech.* **208**, 67–89.

PHINNEY, R. E. 1975 Breakup of a turbulent liquid in a low-pressure atmosphere. *AIChE J.* **21**, 996–999.

PLATEAU, J. 1873 *Soumis aux Seules Forces Moleculaires*, vol. 2. Gauthier-Villars.

RANZ, W. E. 1958 Some experiments on orifice sprays. *Can. J. Chem. Engng* **36**, 175–181.

RAYLEIGH, LORD 1878 On the instability of jets. *Proc. Lond. Math. Soc.* **10**, 4–13.

RAYLEIGH, LORD 1880 On the stability, or instability, of certain fluid motions. *Proc. Lond. Math. Soc.* **12**, 57–70.

RAYLEIGH, LORD 1883 Investigation of the character of the equilibrium of an incompressible heavy fluid of variable density. *Proc. R. Soc.* **14**, 170–177.

REES, S. J. & JUNIPER, M. P. 2009 The effect of surface tension on the stability of unconfined and confined planar jets and wakes. *J. Fluid Mech.* **633**, 71–97.

REITZ, R. D. & BRACCO, F. V. 1982 Mechanism of atomization of liquid jets. *Phys. Fluids* **25**, 1730–1742.

SCHLICHTING, H. 1968 *Boundary-Layer Theory*. McGraw-Hill.

SHINJO, J. & UMEMURA, A. 2010 Simulation of liquid jet primary breakup: dynamics of ligament and droplet formation. *Intl J. Multiphase Flow* **36**, 513–532.

SHINJO, J. & UMEMURA, A. 2011 Surface instability and primary atomization characteristics of straight liquid jet sprays. *Intl J. Multiphase Flow* **37**, 1294–1304.

STERLING, A. M.. & SLEICHER, C. A. 1975 The instability of capillary jets. *J. Fluid Mech.* **68**, 477–495.

TAKEMOTO, Y. & MIZUSHIMA, J. 2010 Mechanism of sustained oscillations in a fluid flowing past a circular cylinder obstacle. *Phys. Rev.* E **82**, 056316.

TAYLOR, G. I. 1950 Hydrodynamic instabilities. *Proc. R. Soc. Lond.* A **201**, 192–196.

TAYLOR, G. I. 1963 Generation of ripples by wind blowing over a viscous liquid. In *The Scientific Papers of Sir Geoffrey Ingram Taylor* (ed. G. K. Bachelor), vol. III, pp. 244–254. Cambridge University Press.

TAYLOR, J. J. & HOYT, J. W. 1983 Water jet photography – techniques and methods. *Exp. Fluids* **1**, 113–120.

TAYLOR, M. J. & PEAKE, N. 1999 A note on the absolute instability of wakes. *Eur. J. Mech. (B/Fluids)* **18**, 573–579.

TRINH, H. P. 2007 Modeling of turbulence effect on liquid jet atomization. NASA/TM-2007-215189.

UMEMURA, A. 2011 Self-destabilizing mechanism of a laminar inviscid liquid jet issuing from a circular nozzle. *Phys. Rev.* E **83**, 046307.

UMEMURA, A., KAWANABE, S., SUZUKI, S. & OSAKA, J. 2011 Two-valued breakup length of a water jet issuing from a finite-length nozzle under normal gravity. *Phys. Rev.* E **84**, 036309.

VILLERMAUX, E. & CLANET, C. 2002 Life of a flapping liquid sheet. *J. Fluid Mech.* **462**, 341–363.

WOOD, W. R. & LOOMIS, A. L. 1927 Physical and biologic effects of high frequency sound waves of great intensity. *Phil. Mag.* **4**, 417–437.

WOODLEY, B. M. & PEAKE, N. 1997 Global linear stability analysis of thin aerofoil wakes. *J. Fluid Mech.* **339**, 239–260.

WU, P.-K., MIRANDA, R. F. & FAETH, G. M. 1995 Effect of initial flow conditions on primary breakup of nonturbulent and turbulent round liquid jets. *Atomiz. Sprays* **5**, 175–196.

WU, P.-K., TSENG, L.-K. & FAETH, G. M. 1992 Primary breakup in gas/liquid mixing layers for turbulent liquids. *Atomiz. Sprays* **2**, 295–317.

YECKO, S. & ZALESKI, S. 2005 Transient growth in two-phase mixing layers. *J. Fluid Mech.* **528**, 43–52.

YECKO, P., ZALESKI, S. & FULLANA, J. M. 2002 Viscous modes in two-phase mixing layers. *Phys. Fluids* **14**, 4115–4122.

YU, M.-H. & MONKEWITZ, P. A. 1990 The effect of non-uniform density on the absolute instability of planar inertial jets and wakes. *Phys. Fluids* A **2** (7), 1175–1181.